MODELING THE EFFECTS OF INDUCTION HEATING ON ARBITRARY SHAPE MEMORY ALLOY COMPONENTS

A Thesis

by

ROBERT N. SAUNDERS

Submitted to the Office of Graduate and Professional Studies of
Texas A&M University
in partial fulfillment of the requirements for the degree of

MASTER OF SCIENCE

Chair of Committee,	Dimitris C. Lagoudas
Co-Chair of Committee,	James G. Boyd
Committee Members,	Darren Hartl
	Richard Malak
Head of Department,	Rodney Bowersox

August 2015

Major Subject: Aerospace Engineering

ABSTRACT

The present work examines the effects of high frequency induction heating on shape memory alloy (SMA) components with arbitrary geometries. SMA actuators deliver high forces but are compact and reliable, making them ideal for consideration in aerospace applications. One disadvantage of these thermally driven actuators is their slow time response compared to conventional actuators. By subjecting the SMA component to electromagnetic fields such as those in induction heating enables the component to be heated in seconds. Although induction heating has recently been used to quickly heat SMA components, efforts to date have been purely empirical. This work presents the governing electromagnetic, thermo-mechanical, and constitutive equations needed to approach the problem in a computational manner. The derived equations are implemented in a finite element framework, which can be used for any 3-D arbitrary coil or SMA geometry and relative positioning. The time-harmonic electromagnetic equations are solved for the Joule heat power field, and then the energy and linear momentum equations are solved for the temperature and displacement fields. The 3-D model is implemented in the Abaqus Unified FEA software using a Python script approach and applied to two example cases: an SMA torque tube and an SMA bending beam actuator. The torque tube model is validated against induction heating experiments and agrees well. A study of flux concentrator properties and positions relative to the SMA actuator is shown, which demonstrates a reduction in the time required to heat. To accommodate future optimization work, the developed model is reduced from 3-D to an ordinary differential equation (ODE) in time for the case of a thin walled SMA torque tube, which assumes negligible gradients in all fields. The ODE solution agrees well with experiments and is able to

capture the deviations from linearity due to latent heat effects.

DEDICATION

To my family:

my mother Donna,

my grandparents Nelson and Gloria,

my fiancée Faith

ACKNOWLEDGEMENTS

I first want to thank my family for their support and guidance through all of my life. Without my mother and grandparents constant encouragement I would not be where I am today.

I would next like to thank all of my advisers over the years of undergraduate and graduate research. My first research endeavor as an undergraduate was with Dr. Seidel at Virginia Tech, who introduced me to shape memory alloys. Without his guidance, I would not have even considered continuing my education after a bachelor's degree and definitely would not have chosen to move across the country to Texas A&M.

At Texas A&M, I had the pleasure of working with many great researchers in the SMART research group. These students researchers always helped spark new ideas on how to complete research tasks. Of course I would be remiss if I did not mention my research advisers who guided me through the toughest two years of work I have experienced. Drs. Boyd and Hartl constantly made time to meet with me and provide me with guidance on all of my projects. Without their help, I would not have the knowledge and research experience that I possess today and for that I am thankful. I would also like to thank Dr. Lagoudas who continuously challenged me to do more and think deeply about everything I was doing. After being advised by him for two years I see everything in an entirely new perspective and know that nothing should be accepted at face value. Dr. Lagoudas' guidance has led me to position at the U.S. Naval Research Lab so that I may begin a career in engineering research and has given me the motivation to become a leader in engineering.

My time at Texas A&M has largely been supported by The Boeing Company.

This experience has been invaluable. Working with Tad Calkins, Jonathan Brown, Mike Gamble, and many others has been an absolute pleasure. The feedback and support they provided me throughout this entire process has allowed me to work on this challenging project. I'm excited to see where this work goes in continued efforts and hope to see it implemented one day.

Finally, I would like to thank my fiancée and best friend, Faith. She has been a constant source of love and support in my life and always encouraged me to do more. She constantly listened to the ups and downs of my research and always knew exactly what to say. She is the reason I have been able to make it this far.

TABLE OF CONTENTS

Page

LIST OF FIGURES

FIGURE Page

LIST OF TABLES

TABLE Page

1. INTRODUCTION

Shape memory alloys (SMAs) are active materials that provide lightweight, compact actuation with a high volume-specific mechanical energy density. SMAs can recover strains as large as 10% due to changes in temperature and/or stress [46]. The inelastic recoverable strain generated in the SMA is commonly referred to as transformation strain, or actuation strain. This transformation strain is due to a diffusionless solid-to-solid transformation from a parent phase (austenite) to one or more crystallographic variants of martensite [62]. Although there is only a single variant of austenite, there can be many variants of martensite [8]. These martensite variants can be oriented under the appropriate application of stress and temperature, resulting in reconfigurable strains that can be recovered during martensitic transformation. This is known as the shape memory effect (SME) and provides a solid-state alternative in general actuation applications. The SME must be trained in the SMA by thermo-mechanically cycling the actuator under load in the direction of desired actuation until a stable hysteresis is achieved. Based on a number of factors, training may result in an SMA component that favors a particular internal distribution of oriented martensite variants. This is known as the two-way SME, which is the ability of the SMA to exhibit substantial actuation deformations between set configurations in both the austenite and martensite phases, even under no loading. The most common form of SMA actuator is wire, which can actuate in a uniaxial tensile manner and, when they are formed into extensional springs, in a locally torsional manner. If actuation is desired in other directions, systems can be devised that allow these wires to be used, but such systems can become complex and inefficient in terms of volumetric energy density. To provide an alternative to wire-based solutions, recent

developments have shown that SMA material can be processed and trained as large specimens with the ability to bend and twist under substantial loads [28].

1.1 SMA Torque Tubes and Bending Beams

SMA torsional actuators, commonly torque tubes, can be used for large-scale applications. SMA torque tubes are particularly useful for actuation in aerospace applications such as wing twisting [74, 76, 35], rotor blade twisting [65, 44], and space based radiator morphing [4, 15]. Since the primary mode of operation in SMA tubes is not tensile, the methods traditionally used to characterize SMA wires are not applicable. Many authors have developed reliable methods which are able to accurately characterize [51, 43] and model [50, 53] the behavior of torque tubes under a variety of thermal and mechanical loading conditions. In addition to torsional actuators, SMA bending beams have found application in the aerospace community. These beams have been characterized and modeled for a variety of aircraft [31, 32] and spacecraft [13, 68] applications as well as structural damping applications [18] beyond the aerospace industry.

1.2 SMA Heating Methods

While SMAs have a very high volumetric energy density compared to other actuators their actuation rate and frequency is limited by how quickly heat can be added and removed from the SMA component. Many authors suggest methods of heating and cooling [78, 86, 67], some of which are summarized in table 1.1.

Table 1.1: Potential heating and cooling methods for shape memory alloys actuator components.

Heating	**Cooling**
Direct resistive [9, 37, 85, 63, 67]	Free convection (air) [87]
Conductive [31]	Liquid immersion [22]
Convective [22]	Forced air/liquid convection [87]
Radiative (including laser) [38, 52]	Peltier effect [80]
Inductive [88]	Heat sinking [3]
Chemical [57, 40, 41]	*Cool Chips* technology [78]

The size of the SMA body greatly affects the choice of heating and cooling system implemented. Direct resistive heating is accepted as the most efficient heating method but such a method is generally current-limited to small and slender (i.e. wire) implementations [49]. For these large pieces, conductive and inductive heating become the best options. The speed of conductive heating is limited by distance (i.e. part size) and thermal conductivity, which is quite low in SMAs[1]. When trying to heat quickly inductive and chemical options are both effective. Chemical heating through combustion is able to heat at extreme rates but, for obvious reasons, is not feasible in applications intended for aerospace applications, which are of interest here. Inductive heating then becomes the optimal option to heat a large SMA component in a short time.

[1]Approximately 5% that of a pure aluminum [36]

1.3 Induction Heating

Induction heating is a non-contact heating method whereby an alternating current is input to a coil, inducing a time-harmonic electromagnetic field surrounding the coil. An electrically conductive workpiece in the vicinity of the coil and its field experiences an induced internal current at the same frequency as the exciting frequency but having an opposite flow of current [69].

Induction heating is commonly used in industrial manufacturing processes such as forging, material forming, heat treatment, or melting [77]. The frequency utilized is relatively high ($\approx 10^4 - 10^6$ Hz (or 1/s)). Induction heating offers benefits over other heating methods in terms of control because the heating process can be nearly instantaneously started/stopped, the heating rate is rapid, and the results are consistent over each cycle of heating. The induced currents, known as *eddy currents*, result in a localized Joule heating effect in the workpiece. The induced currents are spatially non-uniform; their distribution depends on the workpiece electromagnetic properties, eddy current frequency, and proximity of the workpiece to the coil. The combination of these parameters affects the depth to which the magnetic field can penetrate the workpiece, known as the *skin effect*. A result of this skin effect is that 86% [20] of the heating power is often concentrated on the surface of a large conducting workpiece and the magnitude of the magnetic field decays exponentially as the distance from the surface increases as shown in figure 1.1.

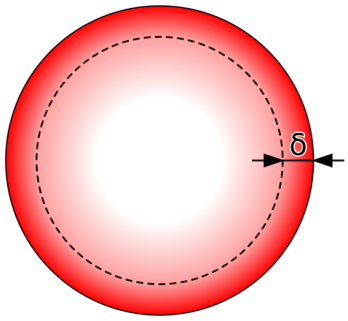

Figure 1.1: Skin effect shown on a solid cylindrical body.

The penetration depth δ is defined as the distance from the workpiece surface at which the magnetic field has decayed to e^{-1} times its surface value [20] and is given by:

$$\delta = \sqrt{\frac{\rho}{\pi \mu_0 \mu_r f}}, \tag{1.1}$$

where ρ is the electrical resistivity, μ_0 is the magnetic permeability of vacuum ($4\pi \times 10^{-7}$ H/m), μ_r is the relative magnetic permeability, and f is the frequency in Hz of the current.

Induction heating has recently been applied to a number of active material applications in an experimental manner. For example, work with shape memory polymers has shown that magnetic nanoparticles embedded in the polymer matrix allow the material to achieve faster heating and in turn faster actuation [55, 10]. In alloy manufacturing, induction heating is used as a method to quickly and cheaply melt pure metals (i.e. Ni-pellets and Ti-rods); in SMA production, this yields a material that has a better chemical homogeneity relative to other methods [42, 12, 24]. Induction heating has been implemented in SMA medical device applications as it offers a method of non-contact heating whereby only the SMA component is heated while the

surrounding material is not [75, 25, 83, 14]. Outside of the medical device industry, Hamilton et al. used induction heating to heat grips for testing a single crystal SMA specimen [26], Wetzel used induction heating to actuate an SMA piece in a controlled de-bonding application [90], and Webster most notably considered induction heating on SMA components associated with an adaptable turbine exhaust [88, 6]. To fully understand how active materials and induction heating interact, predictive analytical/computational studies of SMA components in an electromagnetic field is desired. Takagi et al. [82] showed simulations of an electromagnetic field in an SMA plate using a phenomenological model, but that work does not develop such a model for a general component.

1.4 Magnetic Flux Concentrators

In induction heating, it is common to introduce a high permeability, high resistivity material into the system in close proximity to the induction coil. This material is known as a magnetic flux concentrator (MFC) (also called flux intensifier, diverter, or controller) [69]. MFCs operate by what is referred to as the electromagnetic slot effect illustrated by figure 1.2. The slot effect redistributes the electromagnetic fields around the workpiece and concentrates them though the open surface of the magnetic flux concentrator. Furthermore these MFCs have the effect of preventing the spread of electromagnetic power that otherwise would not contribute to heating the workpiece [69].

The local increase in magnetic field leads to an increased electrical efficiency as well as an increase in heating rate [91]. Other benefits of implementing MFCs include but are not limited to improvements in coil matching to power sources, protection of other equipment in the vicinity from electric and magnetic fields, and improvements in the coil power factor [71]. MFCs are commonly made of magnetic alloy lami-

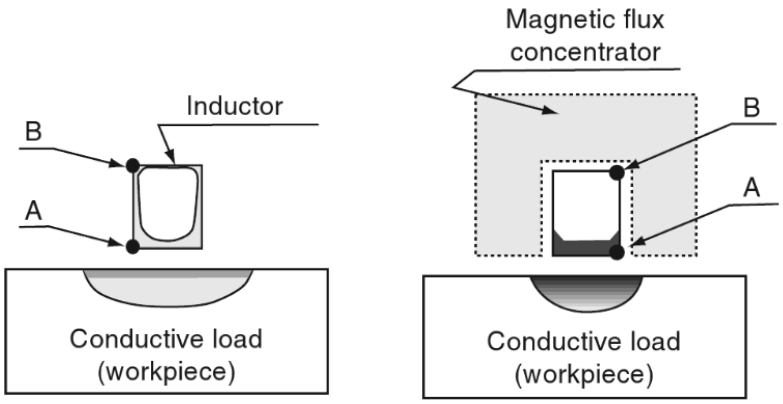

(a) Current distribution in a workpeice without a flux concentrator.

(b) Redistirbution of current in the workpiece due to the slot effect.

Figure 1.2: Current redistribution in an electrically conductive workpiece due to the addition of a magnetic flux concentrator [69].

nations, magneto-dielectrics [72], or ferritic materials [70], where each has specific advantages and disadvantages and work best in a specific frequency range. The benefits of introducing MFCs to an induction system are numerous but there are some caveats associated with the use of MFCs. The MFC will, in operation, experience large magnetic fields, which can degrade the magnetic properties and generate body forces that over time can be problematic. MFCs also consist of magnetic particles, commonly iron, which have the tendency to rust and typically have large mass.

1.5 Outline of the Thesis

The current research aims to investigate the effects of electromagnetic induction heating on general SMA bodies in a computation manner for the first time. The remainder of the thesis is organized as follows:

Section 2 will develop the governing equations need to describe both the electromagnetic, thermo-mechanical, and constitutive behavior of the SMA. This includes a discussion of the implementation. The derived equations will be

reduced from a partial differential equation in space and time to an ordinary differential equation (ODE) in time for use in a thin walled tube problem where it will be assumed no gradients exist.

Section 3 shows the detailed electromagnetic and thermo-mechanical material constant determination for an SMA tube. The constants are found using FEA and verified with the ODE solution.

Section 4 demonstrates the effectiveness of the developed FE model on two cases: an SMA torque tube and SMA bending beam actuator. In the case of the SMA tube, two experiments are completed to verify the model. The first varies the input power to the induction system to show that the developed model is able to capture the measured behavior. The second uses active cooling to achieve high rate actuation and show that the FE model is able to predict the behavior at high rates. Both of the experiments and corresponding FEA results are compared to the ODE solution. Following the validation, the FE model is used to study the effects of frequency through the tubes thickness. Finally, the FE model is implemented in a bending beam study and a study on the effects of flux concentrators.

Section 5 summarizes and concludes the work, and suggestions for future work are given.

2. GOVERNING EQUATIONS

The objective in analyzing an SMA actuator is to understand the spatial and temporal distributions of stresses, strains, and temperature throughout the body. The necessary equations to model these fields are presented in this chapter. In this work all material properties are assumed to be isotropic. In this work small deformations are assumed so that the material time derivative d/dt can be replaced by the local time derivative $\partial/\partial t$, which is denoted by an overhead dot i.e. $\dot{(\ )}$. The magnitude of a vector is denoted as $|\cdot|$ where the magnitude is given by $\sqrt{(\cdot)^2}$ for a real vector and $(\cdot)(\cdot)^*$ for a complex vector where * denotes the complex conjugate.

2.1 Physical Principles

In general the conservation of linear momentum [7] requires universal local satisfaction of

$$\nabla \cdot \boldsymbol{\sigma} + \boldsymbol{f} = 0, \tag{2.1}$$

where $\boldsymbol{\sigma}$ is the (symmetric) Cauchy stress tensor. However in this work, the electromagnetic [84] and gravitation body forces

$$\boldsymbol{f} = \rho^c \boldsymbol{E} + (\nabla \boldsymbol{E})\,\boldsymbol{P} + \boldsymbol{J} \times \boldsymbol{B} + (\boldsymbol{B}\nabla)^T \boldsymbol{M} + \rho^m \boldsymbol{g} \tag{2.2}$$

are assumed to be negligible. In these equations, ρ^c is the free electric charge density, $\boldsymbol{E}$ is the electric field intensity, $\boldsymbol{P}$ is the polarization, $\boldsymbol{J}$ is the current density, $\boldsymbol{B}$ is the magnetic flux density, $\boldsymbol{M}$ is the magnetization, ρ^m is the mass density, and $\boldsymbol{g}$ is the gravitational constant. It should be noted that in electromagnetics, body moments exist of the form [84, 21]

$$\boldsymbol{m} = \boldsymbol{P} \times \boldsymbol{E} + \boldsymbol{M} \times \boldsymbol{B}, \tag{2.3}$$

but in this work they are assumed to be negligible as with the body forces. The linear strain-displacement equations [7] are used as

$$\boldsymbol{\varepsilon} = \frac{1}{2}\left[\nabla \boldsymbol{u} + (\nabla \boldsymbol{u})^T\right], \tag{2.4}$$

where $\boldsymbol{\varepsilon}$ is the total strain tensor and $\boldsymbol{u}$ is the displacement vector. The first law of thermodynamics is written as

$$\rho^m \dot{u} = \boldsymbol{\sigma} : \dot{\boldsymbol{\varepsilon}} + \boldsymbol{E} \cdot \dot{\boldsymbol{D}} + \boldsymbol{H} \cdot \dot{\boldsymbol{B}} + \boldsymbol{E} \cdot \boldsymbol{J} - \nabla \cdot \boldsymbol{q}, \tag{2.5}$$

where u is the specific internal energy, $\boldsymbol{H}$ is the magnetic field intensity, $\boldsymbol{D}$ is the electric displacement, and $\boldsymbol{q}$ is the conduction heat flux vector. In addition to the first law, the second law must be used to develop thermodynamically consistent constitutive equations. The second law can be written in the form of the Clausius-Planck inequality [46] as

$$\rho^m \dot{s} + \nabla \cdot \boldsymbol{q} \geq 0, \tag{2.6}$$

where s is the entropy. When an SMA body is subjected to time varying electromagnetic fields such as those in induction heating, Maxwell's equations in the local form are needed and are given in full form as [69, 73, 89]

$$\nabla \times \boldsymbol{H} = \boldsymbol{J} + \dot{\boldsymbol{D}} \qquad \text{(Ampere's Law)}\ , \tag{2.7a}$$

$$\nabla \times \boldsymbol{E} = -\dot{\boldsymbol{B}} \qquad \text{(Faraday's Law)}\ , \tag{2.7b}$$

$$\nabla \cdot \boldsymbol{B} = 0 \qquad \text{(Gauss' Law for Magnetism)}\ , \tag{2.7c}$$

$$\nabla \cdot \boldsymbol{D} = \rho^c \qquad \text{(Gauss' Law)}\ . \tag{2.7d}$$

2.2 Constitutive Equations

A Gibbs free energy is chosen with the following independent variables, $G = G\left(\boldsymbol{\sigma}, T, \boldsymbol{D}, \boldsymbol{B}, \boldsymbol{\varepsilon}^t, \xi, g^t\right)$, where T is the temperature, $\boldsymbol{\varepsilon}^t$ is the transformation strain tensor, ξ denotes the martensite volume fraction, and g^t is the transformation hardening energy. The Coleman-Noll procedure [16, 17] can be applied to derive

$$s = -\frac{\partial G}{\partial T}, \tag{2.8a}$$

$$\boldsymbol{\varepsilon} = -\rho^m \frac{\partial G}{\partial \boldsymbol{\sigma}}, \tag{2.8b}$$

$$\boldsymbol{E} = \rho^m \frac{\partial G}{\partial \boldsymbol{D}}, \tag{2.8c}$$

$$\boldsymbol{H} = \rho^m \frac{\partial G}{\partial \boldsymbol{B}}. \tag{2.8d}$$

Application of the second law of thermodynamics results in a dissipation inequality, which is assumed to be able to be decomposed into the following three inequalities

$$\boldsymbol{E} \cdot \boldsymbol{J} \geq 0, \tag{2.9a}$$

$$-\boldsymbol{q} \cdot \nabla T \geq 0, \tag{2.9b}$$

$$\frac{\partial G}{\partial \boldsymbol{\varepsilon}^t} : \dot{\boldsymbol{\varepsilon}}^t + \frac{\partial G}{\partial \xi}\dot{\xi} + \frac{\partial G}{\partial g^t}\dot{g}^t \geq 0. \tag{2.9c}$$

The first two inequalities are able to be decoupled by neglecting thermal electric effects (Seebeck and Peltier) and the third represents the generalized thermodynamical forces [48, 46]. The form of the free energy is chosen so that an electric constitutive

relation, a magnetic constitutive relation, Ohm's law, and Fourier's law are given by

$$\boldsymbol{D} = \epsilon_0 \epsilon_r \boldsymbol{E}, \tag{2.10a}$$

$$\boldsymbol{B} = \mu_0 \mu_r \boldsymbol{H}, \tag{2.10b}$$

$$\boldsymbol{E} = \rho \boldsymbol{J}, \tag{2.10c}$$

$$\boldsymbol{q} = -k \nabla T. \tag{2.10d}$$

where k is the thermal conductivity, ϵ_0 is the permittivity of free space, and ϵ_r is the relative permittivity.

There are many constitutive models that describe SMA behavior [64, 47]. The model chosen herein was developed by Lagoudas et al. [8, 46, 48]. This model is computationally efficient and has been proven experimentally accurate under a variety of thermo-mechanical loading conditions [30]. The core model is the plasticity model of Hartl et al. [29] and has been modified to account for transformation induced anisotropy by Solomou et al. [33, 27].

Because the electromagnetic and thermo-mechanical terms in the free energy are assumed to be uncoupled, the thermo-mechanical specific Gibbs free energy due to the austenite, martensite, and mixed phases is given by the rule of mixtures as

$$\begin{aligned} G^{SMA}\left(\boldsymbol{\sigma}, T, \boldsymbol{\varepsilon}^t, \xi, g^t\right) &= G^A\left(\boldsymbol{\sigma}, T\right) + \\ \xi\left[G^M\left(\boldsymbol{\sigma}, T\right) - G^A\left(\boldsymbol{\sigma}, T\right)\right] &+ G^{mix}\left(\boldsymbol{\sigma}, \boldsymbol{\varepsilon}^t, g^t\right). \end{aligned} \tag{2.11}$$

G^A and G^M represent the Gibbs free energy in the austenite and martensite phases

respectively. Assuming a quadratic stress dependence, G^{ζ} for $\zeta = A, M$ gives

$$\begin{aligned} G^{\zeta}(\boldsymbol{\sigma}, T) = -\frac{1}{2\rho^m}\boldsymbol{\sigma} : \boldsymbol{S}^{\zeta}\boldsymbol{\sigma} - \frac{1}{\rho^m}\boldsymbol{\sigma} : \boldsymbol{\alpha}^{\zeta}(T - T_0) + \\ c^{\zeta}\left[(T - T_0) - T\ln\left(\frac{T}{T_0}\right)\right] - s_0^{\zeta}T + u_0^{\zeta} \end{aligned} \tag{2.12}$$

and the mixing term is given as

$$G^{mix}\left(\boldsymbol{\sigma}, \boldsymbol{\varepsilon}^t, g^t\right) = -\frac{1}{\rho^m}\boldsymbol{\sigma} : \boldsymbol{\varepsilon}^t + \frac{1}{\rho^m}g^t. \tag{2.13}$$

The parameters $\boldsymbol{S}$, T_0, s_0, and u_0 are the compliance tensor, reference temperature, specific reference entropy, and specific reference internal energy. The values of $\boldsymbol{S}$, s_0, and u_0 are all assumed to be dependent on the phase of the material. The specific heat c, density ρ^m, and the second-order coefficient of thermal expansion $\boldsymbol{\alpha}$ are assumed constant regardless of phase. The phase-dependent parameters are evaluated by a rule of mixtures in terms of ξ. For example, the compliance tensor $\boldsymbol{S}(\xi)$ is found as

$$\boldsymbol{S}(\xi) = \boldsymbol{S}^A + \xi\left(\boldsymbol{S}^M - \boldsymbol{S}^A\right) = \boldsymbol{S}^A + \xi\tilde{\boldsymbol{S}}. \tag{2.14}$$

Now using the procedure of Coleman-Noll, the total strain and entropy are obtained as

$$\boldsymbol{\varepsilon} = -\rho^m\frac{\partial G}{\partial \boldsymbol{\sigma}} = \boldsymbol{S}(\xi)\boldsymbol{\sigma} + \boldsymbol{\alpha}(\xi)(T - T_0) + \boldsymbol{\varepsilon}^t \tag{2.15}$$

and

$$s = -\frac{\partial G}{\partial T} = \frac{1}{\rho^m}\boldsymbol{\sigma} : \boldsymbol{\alpha} + c\ln\left(\frac{T}{T_0}\right) + s_0. \tag{2.16}$$

Equation 2.15 can be rewritten in a more common form as Hooke's law,

$$\boldsymbol{\sigma} = \boldsymbol{S}^{-1}\,\boldsymbol{\varepsilon}^{el} = \boldsymbol{S}^{-1}\left[\boldsymbol{\varepsilon} - \boldsymbol{\varepsilon}^t - \boldsymbol{\alpha}(T - T_0)\right]. \tag{2.17}$$

The evolution equations governing the transformation strain and hardening are given as

$$\dot{\boldsymbol{\varepsilon}}^t = \dot{\xi}\boldsymbol{\Lambda}^t\left(\overline{\sigma}^{eff}\right), \tag{2.18a}$$

$$\dot{g}^t = \left[f^t - \boldsymbol{\beta}\boldsymbol{\Lambda}^t\left(\overline{\sigma}^{eff}\right)\right]\dot{\xi}, \tag{2.18b}$$

$$\boldsymbol{\Lambda}^t\left(\overline{\sigma}^{eff}\right) = \begin{cases} \frac{3}{2}H^{cur}\left(\overline{\sigma}^{eff}\right)\frac{\boldsymbol{s}^{eff}}{\overline{\sigma}^{eff}}; & \dot{\xi} > 0 \\ \frac{\boldsymbol{\varepsilon}^{t-r}}{\xi^r}; & \dot{\xi} < 0 \end{cases}, \tag{2.18c}$$

$$H^{cur}\left(\overline{\sigma}^{eff}\right) = H_{max}\left(1 - e^{-k^t\overline{\sigma}^{eff}}\right), \tag{2.18d}$$

$$\boldsymbol{\sigma}^{eff} = \left(\boldsymbol{\sigma} + \boldsymbol{\beta}\right), \tag{2.18e}$$

where H_{max} is the maximum uniaxial transformation strain, $\boldsymbol{s}^{eff}$ is the deviatoric effective stress, $\boldsymbol{\varepsilon}^{t-r}$ is the transformation strain tensor at cycle reversal, ξ^r is the martensitic volume fraction at reversal, $\boldsymbol{\beta}$ is the back stress tensor developed during past training and which does not evolve in this case, k^t is a parameter that controls the rate at which H^{cur} evolves exponentially, σ^{eff} is the Mises equivalent of the effective stress given as

$$\overline{\sigma}^{eff} = \sqrt{\frac{3}{2}\boldsymbol{s}^{eff} : \boldsymbol{s}^{eff}}, \tag{2.19}$$

and f^t is given for forward and reverse transformation as

$$f^t = \begin{cases} \frac{1}{2}a_1\left(1 + \xi^{n_1} - (1-\xi)^{n_3}\right) + a_3; & \dot{\xi} > 0 \\ \frac{1}{2}a_2\left(1 + \xi^{n_3} - (1-\xi)^{n_4}\right) - a_3; & \dot{\xi} < 0 \end{cases}. \tag{2.20}$$

A transformation function constraining the evolution of the martensitic volume frac-

tion is postulated such that

$$\Phi^t = \begin{cases} \Phi^t_{fwd} = \Pi - Y^t; & \dot{\xi} > 0 \\ \Phi^t_{rev} = -\Pi - Y^t; & \dot{\xi} < 0 \end{cases} \tag{2.21}$$

which is constrained in the manner of classical plasticity so that

$$\Phi^t \leq 0, \qquad \dot{\xi}\Phi^t = 0, \qquad 0 \leq \xi \leq 1, \tag{2.22}$$

with the thermodynamic driving force Π given by

$$\Pi\left(\boldsymbol{\sigma}, T, \xi\right) = \boldsymbol{\Lambda}^t : \boldsymbol{\sigma}^{eff} + \frac{1}{2}\boldsymbol{\sigma} : \tilde{\boldsymbol{S}}\,\boldsymbol{\sigma} + \rho^m \tilde{s_0} T - \rho^m \tilde{u_0} - f^t, \tag{2.23}$$

where $\tilde{s_0}$ and $\tilde{u_0}$ are the difference in reference entropy and internal energy, respectively between austenite and martensite. The constant Y^t is a critical value at which transformation occurs, a_1, a_2, and a_3 are transformation hardening coefficients, and $n_1, \ldots, n_4$ are transformation hardening exponents. The parameters $\tilde{s_0}$, $\tilde{u_0}$, Y^t, a_1, a_2, and a_3 can all be expressed in terms of the phase diagram properties M_s, M_f, A_s, A_f, C^A, and C^M [48]. These material properties are to be determined and discussed in more detail in section 3.

The constitutive equations must be further manipulated to determine the effects of the latent heat of phase change. The first law of thermodynamics (equation 2.5) is expanded via equation 2.8b as

$$\rho^m \dot{u} = \boldsymbol{\sigma} : \left(\dot{\boldsymbol{\varepsilon}}^{el} + \boldsymbol{\alpha}\dot{T} + \boldsymbol{\Lambda}\dot{\xi}\right) + \boldsymbol{E} \cdot \boldsymbol{J} + \boldsymbol{E} \cdot \dot{\boldsymbol{D}} + \boldsymbol{H} \cdot \dot{\boldsymbol{B}} - \nabla \cdot \boldsymbol{q}. \tag{2.24}$$

A Legendre transformation is needed to combine and manipulate the Gibbs free

energy and the first and second laws. This transformation is given by

$$\rho^m u = \rho^m G + \boldsymbol{\sigma} : \boldsymbol{\varepsilon} + \rho^m T s. \tag{2.25}$$

Combining equations 2.24 and 2.25 gives

$$T\dot{s} = \frac{1}{\rho^m}\Pi\dot{\xi} + \boldsymbol{E}\cdot\boldsymbol{J} - \nabla\cdot\boldsymbol{q}. \tag{2.26}$$

Now the definition of entropy is used to write

$$\boldsymbol{E}\cdot\boldsymbol{J} - \nabla\cdot\boldsymbol{q} = -T\left(\frac{\partial^2 G}{\partial\boldsymbol{\sigma}\partial T}\dot{\boldsymbol{\sigma}} + \frac{\partial^2 G}{\partial T^2}\dot{T}\right) - \left[T\left(\frac{\partial^2 G}{\partial\xi\partial T} + \frac{\partial^2 G}{\partial\boldsymbol{\varepsilon}^t\partial T}\boldsymbol{\Lambda}\right) + \frac{1}{\rho^m}\Pi\right]\dot{\xi}. \tag{2.27}$$

In equation 2.27, $\dot{\xi}$ is eliminated using the fact that $\dot{\Pi} = 0$ during transformation [8], which yields

$$\dot{\xi} = \left(-\frac{\partial\Pi}{\partial\xi}\right)^{-1}\left(\frac{\partial\Pi}{\partial\boldsymbol{\sigma}}\dot{\boldsymbol{\sigma}} + \frac{\partial\Pi}{\partial T}\dot{T}\right). \tag{2.28}$$

Substituting equation 2.28 reduces equation 2.27 to

$$\boldsymbol{E}\cdot\boldsymbol{J} - \nabla\cdot\boldsymbol{q} = \left(\frac{1}{\rho^m}\boldsymbol{\alpha}T - \mathfrak{D}\frac{\partial\Pi}{\partial\boldsymbol{\sigma}}\right) : \dot{\boldsymbol{\sigma}} + \left(c - \mathfrak{D}\frac{\partial\Pi}{\partial T}\right)\dot{T}, \tag{2.29}$$

where $\mathfrak{D}$ is given by

$$\mathfrak{D} = \left(-\frac{\partial\Pi}{\partial\xi}\right)^{-1}\left[\frac{1}{\rho^m}\Pi - T\left(\frac{1}{\rho^m}\tilde{\boldsymbol{\alpha}} : \boldsymbol{\sigma} + \tilde{c}\ln\left(\frac{T}{T_0}\right) + \tilde{s_0}\right)\right]. \tag{2.30}$$

If transformation is not occurring (i.e. $\dot{\xi} = 0$), equation 2.29 reduces to simply

$$\boldsymbol{E}\cdot\boldsymbol{J} - \nabla\cdot\boldsymbol{q} = \frac{T}{\rho^m}\boldsymbol{\alpha} : \dot{\boldsymbol{\sigma}} + c\dot{T}. \tag{2.31}$$

2.3 Field Equations

The first governing equation combines linear momentum with Hooke's law and the strain-displacement relationship to give the Navier-Cauchy equations[7] written as

$$\nabla \cdot \left[\boldsymbol{C} \left(\nabla \boldsymbol{u} - \boldsymbol{\varepsilon}^t - \boldsymbol{\alpha} \left(T - T_0 \right) \right) \right] = 0. \tag{2.32}$$

Assumptions are made to reduce the previous physical principles and constitutive equations to simpler forms. First, it is assumed that the thermoelastic term $\boldsymbol{\alpha} : \dot{\boldsymbol{\sigma}}$ in the energy equation (2.31) is negligible. Furthermore, the effects of thermo-mechanical coupling due to latent heat are not modeled in the FEA implementation. These effects *are* considered in the ODE solution. The consideration of latent heat in SMA bodies has been considered by various authors including Mirzaeifar et al. [54] who modeled the effects of latent heat on the response of SMA rods of circular cross section under pure torsion and Tabesh et al. [81] who created a model which considers the effects of latent heat in a general 3-D bodies. The work of Tabesh et al. has been used in the computational analysis of SMA wires and a computational design optimization of 3-D aerostructures [61]. The current FE model is developed to be applicable to arbitrary geometries, similar to the previously mentioned models, with arbitrary distributions of Joule heating, which can have large gradients. To this effect, the FE model is simplified by neglecting the effects of latent heat and reduce equation 2.29 to

$$\frac{1}{2} \rho \boldsymbol{J} \cdot \boldsymbol{J} + k \nabla^2 T = c \dot{T}, \tag{2.33}$$

which is subject to the convection boundary condition given by

$$-k \frac{\partial T}{\partial \boldsymbol{n}} = h \left(T_s - T_\infty \right), \tag{2.34}$$

where h is the convection coefficient, T_s is the surface temperature, T_∞ is the ambient temperature, and $\boldsymbol{n}$ is the unit normal to the boundary.

To reduce Maxwell's equations to a form that can be implemented in a finite element method, an equation based on the current in the coil is derived. To describe a vector field fully, both its divergence and curl must be uniquely defined. From Gauss' law for magnetism, the magnetic flux density has zero divergence such that it is represented by the curl of another vector $\boldsymbol{A}$ as

$$\boldsymbol{B} = \nabla \times \boldsymbol{A}, \tag{2.35}$$

where $\boldsymbol{A}$ is known as the magnetic vector potential. Now from Faraday's law, it follows that

$$\nabla \times \boldsymbol{E} = -\nabla \times \dot{\boldsymbol{A}} \tag{2.36}$$

or

$$\nabla \times \left(\boldsymbol{E} + \dot{\boldsymbol{A}}\right) = 0. \tag{2.37}$$

The curl of the gradient of any scalar field is always the zero vector (i.e. $\nabla \times (\nabla\phi) = \boldsymbol{0}$). This identity can now be applied to the previous equation to give

$$\boldsymbol{E} = -\dot{\boldsymbol{A}} - \nabla\phi, \tag{2.38}$$

where ϕ is the electric scalar potential. Now using the magneto-quasi-static approximation ($\dot{\boldsymbol{D}} = 0$) and substituting Ohm's law into Ampere's law gives

$$\nabla \times \boldsymbol{H} = \frac{1}{\rho}\left(-\dot{\boldsymbol{A}} - \nabla\phi\right), \tag{2.39}$$

into which the constitutive equation for $\boldsymbol{H}$ and the magnetic vector potential are

substituted to yield

$$\nabla \times \nabla \times \frac{\boldsymbol{A}}{\mu_0 \mu_r} = -1/\rho \left(\dot{\boldsymbol{A}} + \nabla \phi \right). \tag{2.40}$$

The source current is defined as $\boldsymbol{J}_s = -1/\rho \nabla \phi$. As is common in induction heating, the excitation is considered to be sinusoidal giving $\boldsymbol{A} = \boldsymbol{A}_0 e^{j\omega t}$ and $\dot{\boldsymbol{A}} = j\omega \boldsymbol{A}$, where $\boldsymbol{A}_0$ contains the magnitude and phase angle of $\boldsymbol{A}$. The same procedure can be done for $\boldsymbol{J}_s$ to give $\boldsymbol{J}_s = \boldsymbol{J}_{s0} e^{j\omega t}$. Combining the previous equations gives

$$\nabla \times \nabla \times \frac{\boldsymbol{A}_0 e^{j\omega t}}{\mu_0 \mu_r} + \frac{j\omega}{\rho} \boldsymbol{A}_0 e^{j\omega t} = \boldsymbol{J}_{s0} e^{j\omega t}. \tag{2.41}$$

Assuming that the electromagnetic properties of the material do not vary spatially allows equation 2.42 to be rewritten as

$$\frac{1}{\mu_0 \mu_r} \nabla \times \nabla \times \boldsymbol{A}_0 + \frac{j\omega}{\rho} \boldsymbol{A}_0 = \boldsymbol{J}_{s0}, \tag{2.42}$$

which helps to formulate a simple weak form equation for the finite element implementation. The boundary conditions on the vector potential are simple because they decay to a small value far away from the workpiece such that the magnetic vector potential can be set equal to zero in the numerical implementation. The source current term $\boldsymbol{J}_{s0}$ in equation 2.42 corresponds to a simple current measurement. Now with the single measurement of a single input quantity and a sufficiently large finite element problem domain, the source term and the boundary conditions have been defined and the problem is able to be solved.

Returning to Ohm's law (equation 2.10c) with the electric field written in terms of potentials, the current can be decomposed as

$$\boldsymbol{J} = -\frac{1}{\rho} \dot{\boldsymbol{A}} - \frac{1}{\rho} \nabla \phi = -\frac{1}{\rho} \dot{\boldsymbol{A}} + \boldsymbol{J}_s. \tag{2.43}$$

Note that $\boldsymbol{J}$ has both source and induced current contributions expressed as

$$\boldsymbol{J} = \boldsymbol{J}_s + \boldsymbol{J}_e, \tag{2.44}$$

where the induced or eddy current is defined as

$$\boldsymbol{J}_{e0} = -\frac{j\omega}{\rho}\boldsymbol{A}_0, \tag{2.45}$$

and the minus sign indicates that the eddy currents flow in the opposite direction of the source currents. The Joule heating term in equation 2.33 can now be reduced to a source term based on eddy currents [23] so that

$$\frac{1}{2}\rho\boldsymbol{J}_{e0}\cdot\boldsymbol{J}_{e0}^{*} + k\nabla^2 T = c\dot{T}, \tag{2.46}$$

where $\boldsymbol{J}_{e0}^{*}$ is the complex conjugate of $\boldsymbol{J}_{e0}$. Note that $\boldsymbol{J}_{e0}\cdot\boldsymbol{J}_{e0}^{*}$ is equivalent to $|\boldsymbol{J}_{e0}|^2$. When writing equation 2.33, no assumption was made regarding the form of $\boldsymbol{J}$. But here it has been assumed that the current density and therefore the eddy current density is harmonic and thus has real and imaginary parts. Therefore, the complex conjugate must be used in order to account for both the real and imaginary parts of $\boldsymbol{J}_{e0}$. In writing the Joule heating term solely as a function of $\boldsymbol{J}_{e0}$, it is assumed that heating due to electromagnetic hysteresis is negligible compared to eddy currents and that there is no source current applied in the workpiece. Thus with the rate of Joule heating known the remaining thermo-mechanical equations can be solved.

2.4 FE Model Implementation

The governing electromagnetic equation (equation 2.42) is implemented in Abaqus Unified FEA [1]. The SMA constitutive behavior captured in section 2.2 is also im-

plemented in Abaqus via a user material subroutine [66, 45]. In solving the coupled electromagnetic-thermo-mechanical problem of induction heating of SMA components, it is assumed that the problem is one-way coupled and can be solved sequentially; specifically, the electromagnetic problem is solved for a given geometry and input coil current, after which the thermo-mechanical problem is solved considering the generated volumetric heat sources and hysteretic SMA constitutive behavior. This process is similar to the one used by Bay et al. in [2]. In that work, a numerical model was created which considered the thermoelastic-plastic behavior of an axisymmetric workpiece being inductively heated including the variation in magnetic material properties with very large changes in temperature. Here temperature changes are assumed relatively small such that the resistivity and magnetic permeability do not vary with temperature. This assumption allows feedback in the model to eliminated so that the process can be simplified to a one-way (feedforward only) process as illustrated in figure 2.1.

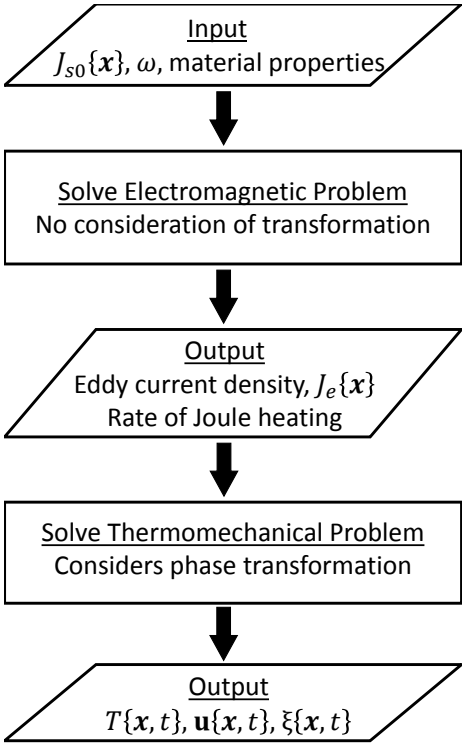

Figure 2.1: Induction heating model flow process.

In the overall engineering model, the coil is assumed to be tightly wound so that it can be considered a continuous sheet as demonstrated by figure 2.2.

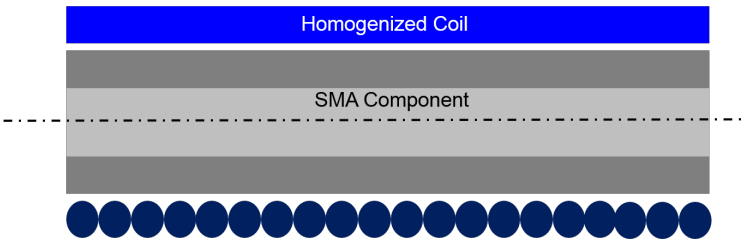

Figure 2.2: Example scenario showing how a tightly wound coil is homogenized into a current sheet.

A consequence of this assumption is that the phase angle between the applied current and voltage is assumed to be strictly 90 degrees (i.e there is no lag in the voltage and current in time.) In an experimental setup a tightly packed coil is typically desired to achieve maximum current density (i.e. faster heating) and a uniform heating distribution along the length of the workpiece.

2.4.1 Mesh Convergence

In addition to the model description of the workpiece and coil geometry, the domain of air or vacuum around the workpiece must be considered. In this work, the initial size of the problem domain is chosen based on the recommendation given in [1] as approximately 10 times the characteristic length scale of the coil and workpiece. In particular, the outer dimension of the domain was chosen such that the field intensity at its boundary was two orders of magnitude less than the field intensity at the point of highest field. The finite element mesh in this domain is globally refined until a converged solution is found then the global mesh is coarsened with local refinements where high gradients exist so that the number of elements, and corresponding analysis time, is reduced while maintaining solution accuracy. Convergence was judged based on the ratio of Joule heating at the outer surface of an SMA tube compared to the inner surface and is shown compared to the number of total elements used in figure 2.3a with the corresponding time taken to run the analysis shown in figure 2.3b. Note that the analysis time is independent of frequency but the number of elements to achieve convergence is not.

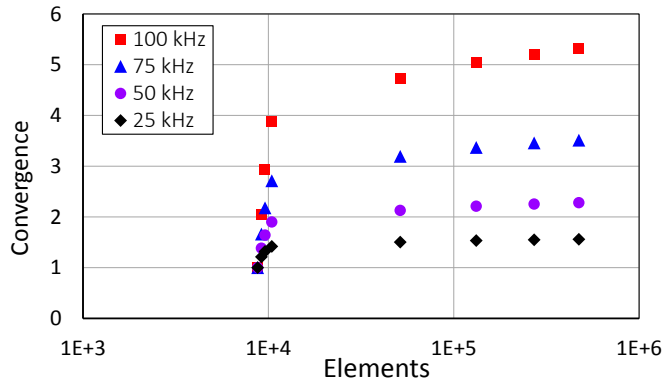

(a) Convergence with number of elements and frequency.

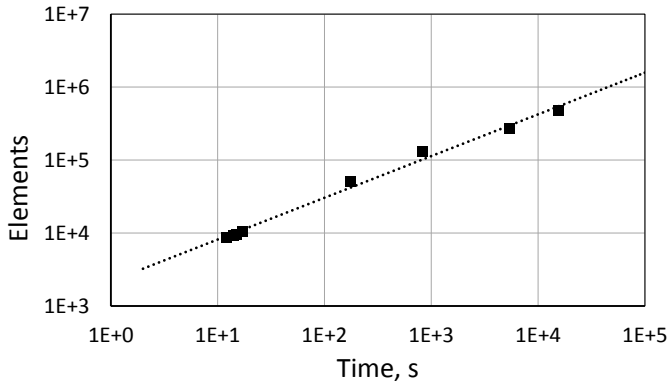

(b) Relationship of analysis time and number of elements.

Figure 2.3: Convergence of the ratio of Joule heating at the outer surface of an SMA tube to the inner surface.

2.4.2 Boundary Conditions

In the electromagnetic problem, a body current density ($\boldsymbol{J}_{s0}$) and frequency are applied in the coil and null magnetic vector potential boundary conditions are applied on the outer domain ($\boldsymbol{A}_0 = 0$). The only electromagnetic material properties required and considered in this implementation are electrical resistivity and magnetic permeability. The coil is modeled as an equivalent current sheet in space, not as an actual material therefor, the resistivity and permeability are considered the same as

vacuum to prevent calculation of eddy currents in the coil [23, 82]. In some electromagnetic modeling implementations, the proposed form of Ohm's law is piece-wise so that $\boldsymbol{J} = 0$ outside of the conducting workpeice [2]. The effects of a piece-wise form of Ohm's law and assuming properties of vacuum in the coil have the same effect, which is numerically preventing eddy currents from being solved in the coil, which is being modeled as only an equivalent current sheet. From the electromagnetic analysis, the nodal location and magnitude of the Joule heating rate are obtained and mapped into the thermo-mechanical problem as a volumetric heat source. This numerical results extraction and mapping is performed using a python script, which is able to extract the required information from the analysis output files.

The thermo-mechanical problem considers the transformation of the SMA component being heated via a volumetric heat source with convective boundary conditions on all SMA surfaces except where the coil is located. The model does not consider thermal conduction or radiation from the coil. From experimental measurements, the coil temperature is known to be approximately equal to the SMA surface temperature throughout the heating process, so an adiabatic boundary condition is used in place of modeling convection at the coil surface or the conduction and radiation between the SMA body and the coil. The outputs of the thermo-mechanical analysis include the temperature and displacement fields as well as the martensitic volume fraction throughout the SMA component.

2.5 Reduction of Governing Equation

One particular application of interest to this work is that of SMA tubes that exhibit a two-way SME that generates twist about the longitudinal axis. Reduced-order solutions exist for both the pseudoelastic torsional behavior of SMA tubes [53] and for induction heating of tubes [20, 49]. It is thus possible to combine these solu-

tions to address the problem of the SMA tube being inductively heated by using an ordinary differential equation in time. In creating this ODE solution, it is assumed that the torque tube is thin walled, axisymmetric, and no end effects exist. These assumption simply correspond to the assumption that no gradients exist in the body. These assumptions substantially reduce the computational cost of the problem compared to the FE model. As mentioned previously, some assumption were made to simplify the FE model, namely, latent heat due to phase transformation was not considered and the resistivity was taken to be phase and temperature independent. In this ODE solution, these effects are reintroduced.

2.5.1 Reduced Electromagnetic Equations [49]

To begin the ODE solution derivation, recall the magneto-quasi-static approximation of Ampere's law (equation 2.39) with Ohm's law substituted.

$$\nabla \times \boldsymbol{H} = \nabla \times \left(\frac{1}{\rho} \boldsymbol{E} \right), \tag{2.47}$$

which can be rewritten as

$$\nabla \left(\nabla \cdot \boldsymbol{H} \right) - \nabla^2 \boldsymbol{H} = \frac{1}{\rho} \nabla \times \boldsymbol{E} + \left(\nabla \frac{1}{\rho} \right) \times \boldsymbol{E}. \tag{2.48}$$

Now Gauss' law for magnetism and Farraday's law with equation 2.10b can be combined to yield

$$\nabla^2 \boldsymbol{H} = \frac{\mu_0 \mu_r}{\rho} \dot{\boldsymbol{H}} - \nabla \left(\boldsymbol{H} \frac{1}{\mu_r} \nabla \mu_r \right) - \rho \left(\nabla \frac{1}{\rho} \right) \times \nabla \times \boldsymbol{H}, \tag{2.49}$$

which can be reduced, assuming a homogeneous permeability and resistivity, to

$$\nabla^2 \boldsymbol{H} = \frac{\mu_0 \mu_r}{\rho} \dot{\boldsymbol{H}}. \tag{2.50}$$

A sinusoidal time-harmonic behavior is again assumed in the electromagnetic fields so that equation 2.50 can be written as

$$\nabla^2 \boldsymbol{H} = j\frac{\omega \mu_0 \mu_r}{\rho} \boldsymbol{H}. \tag{2.51}$$

Equation 2.51 can now be reduced to the case of a cylindrical workpiece by noting that $\boldsymbol{H}$ has only one non-zero component directed along the longitudinal axis of the cylinder and $\boldsymbol{E}$ has only a single non-zero component tangential to the circumference of the cylinder, which reduces the Laplacian of equation 2.51 to only a function of the radial direction r as given by

$$\nabla^2 = \frac{1}{r}\frac{\partial}{\partial r}\left(r\frac{\partial}{\partial r}\right) \tag{2.52}$$

and gives

$$\frac{\partial^2 H_0}{\partial r^2} + \frac{1}{r}\frac{\partial H_0}{\partial r} - j\frac{\omega \mu_0 \mu_r}{\rho} H_0 = 0. \tag{2.53}$$

Equation 2.53, with some manipulation, represents a Bessel differential equation of zero order with general solutions for H_0 and E_0 given by

$$H_0 = C_1 J_0\left(\sqrt{-j} m_r\right) + C_2 Y_0\left(\sqrt{-j} m_r\right), \tag{2.54a}$$

$$E_0 = \sqrt{-2j}\frac{\rho}{\delta}\left[C_1 J_1\left(\sqrt{j} m_r\right) + C_2 Y_1\left(\sqrt{j} m_r\right)\right], \tag{2.54b}$$

where C_1 and C_2 are constants to be determined, J_0 and Y_0 are zero order Bessel

functions of the first and second kind, J_1 and Y_1 are order one modified Bessel functions of the first and second kind, and $m_r = \frac{\sqrt{2}r}{\delta}$. The Bessel functions are implemented in Matlab where the ODE solution is also implemented. For this reason, these Bessel functions are not explicitly listed here. For the problem of a hollow tube with inner radius r_i and outer radius r_e, the boundary conditions needed to solve for C_1 and C_2 are given by

$$H_0 = \begin{cases} H_{e0} = nI; & r = r_e, \\ H_{i0}; & r = r_i, \end{cases} \tag{2.55}$$

where H_{e0} is derived by assuming a long thin wire forms an infinite length solenoid around the tube giving an idealized version of Ampere's law with n being the turns per unit length and I being the peak current input to the coil. Solving for C_1 and C_2 the substituting into equation 2.54 gives

$$H_0 = H_{e0}\frac{F_{00}\left(m_i, m_r\right)}{F_{00}\left(m_i, m_e\right)} - H_{i0}\frac{F_{00}\left(m_e, m_r\right)}{F_{00}\left(m_i, m_e\right)}, \tag{2.56a}$$

$$E_0 = \sqrt{-2j}\frac{\rho}{\delta}\left[H_{e0}\frac{F_{01}\left(m_i, m_r\right)}{F_{00}\left(m_i, m_e\right)} - H_{i0}\frac{F_{01}\left(m_e, m_r\right)}{F_{00}\left(m_i, m_e\right)}\right], \tag{2.56b}$$

where the functions F_{00} and F_{01} are given by

$$F_{00}\left(x, y\right) = J_0\left(\sqrt{-j}y\right)Y_0\left(\sqrt{-j}x\right) - J_0\left(\sqrt{-j}x\right)Y_0\left(\sqrt{-j}y\right) \tag{2.57a}$$

$$F_{01}\left(x, y\right) = J_1\left(\sqrt{-j}y\right)Y_0\left(\sqrt{-j}x\right) - J_0\left(\sqrt{-j}x\right)Y_1\left(\sqrt{-j}y\right) \tag{2.57b}$$

where and x and y are used as place holders. The variables m_i and m_e equal m_r evaluated at r_i and r_e respectively.

In order to determine the radial distribution of H_0 and E_0, H_{i0} must be deter-

mined. The electromotive force (*e.m.f.*) induced in a coil of wire is linked to the change in magnetic field as defined by Faraday's law. This can be applied at the inner surface of the tube to get

$$\oint E_{i0} dl = -A_i \mu_0 \dot{H}_{i0}, \tag{2.58}$$

where A_i is the area enclosed by the inner surface of the tube (πr_i^2) and $\oint E_{i0} dl$ can be evaluated as $2\pi r_i E_{i0}$. Note that the permeability used is not the relative permeability because the previous equation is derived in the internal portion of the tube where there is no material, only air or vacuum. Recall that $\dot{H}_{i0} = j\omega H_{i0}$. Solving 2.58 for E_{i0} and setting this equal to 2.56b evaluated at r_i gives

$$-\frac{j\omega\mu_0 r_i}{2} H_{i0} = \sqrt{-2j}\frac{\rho}{\delta}\left[nI\frac{F_{01}(m_i, m_i)}{F_{00}(m_i, m_e)} - H_{i0}\frac{F_{01}(m_e, m_i)}{F_{00}(m_i, m_e)}\right], \tag{2.59}$$

from which H_{i0} can be determined. With H_{i0} known, the eddy current density J_{e0} can be solved for by application of Ohm's law, which can then be used to find the rate of Joule heating in the tube as was shown in equation 2.46. It should be noted that the determined eddy current density is a function of radius. For the case of a thin walled tube, it is assumed that the eddy current density is approximately constant through the thickness, which gives a comparable result to those published in [20] for thin walled tubes.

2.5.2 Reduced Thermo-Mechanical Equations

With the rate of Joule heating, therefor heating power, known in the tube, the temperature can be solved in time as described by equation 2.27. In order to solve equation 2.27, which considers latent heat due to phase transformation, the constitutive behavior of the SMA must be reduced to an ordinary differential equation

form.

For a tube undergoing pure torsion, the 3-D stress state can be reduced to $\sigma_{23} = \sigma_{32} = \tau$, all other components zero. The shear stress τ can be found by

$$\tau = \frac{T_r d_e}{\frac{1}{32}\pi \left(d_e^4 - d_i^4\right)}, \tag{2.60}$$

where T_r is the torque and d_e and d_i are the outer and inner diameters of the tube. Note that the stress is found at the outer diameter. The stress is taken from this location as it is where the majority of heating will occur first and is the region of most interest.

The SMA model used herein is the same presented in the section 2.2 and detailed in [48, 33]. This model is simplified by considering the reduced stress state in a thin walled tube under torsion and assuming that the stress is time independent. A Gibbs free energy that is identical to the free energy formulated in equations 2.11, 2.12, and 2.13 is used with the exception the thermoelastic term which does not contribute to the shear stress is neglected. This gives a total engineering shear strain γ and entropy as

$$\gamma = \frac{E\left(\xi\right)}{2\left(1+\nu\right)}\tau + \gamma^t, \tag{2.61a}$$

$$s = c \ln\left(\frac{T}{T_0}\right) + s_0. \tag{2.61b}$$

The evolution equations (equation 2.18) are reduced to

$$\dot{\gamma}^t = \dot{\xi}\Lambda^t(\tau), \tag{2.62a}$$

$$\dot{g}^t = \left[f^t - \beta\Lambda^t(\tau)\right]\dot{\xi}, \tag{2.62b}$$

$$\Lambda^t(\tau) = \frac{\sqrt{3}}{2}H^{cur}(\tau), \tag{2.62c}$$

$$H^{cur}(\tau) = 2H_{max}\left(1 - e^{-\sqrt{3}k^t(\tau+\beta)}\right), \tag{2.62d}$$

where β is the 2-3 component of back stress with all others being zero. Note the addition of a 2 in front of equation 2.62d, which has been added to make $H^{cur}(\tau)$ compatible with the engineering strain. In this formulation of the evolution equations, it is assumed that the tube is initially 100% martensite therefor there is not a need to have a forward and reverse component of $\Lambda^t(\tau)$. f^t has not been modified from the form given in equation 2.20. The thermodynamic driving force Π given by equation 2.23 is reduced so that

$$\Pi(\tau, T, \xi) = 2(\tau+\beta)\Lambda^t(\tau) + 4(1+\nu)\tau^2\left(\frac{1}{E_m} - \frac{1}{E_a}\right) + \rho^m\tilde{s_0}T - \rho^m\tilde{u_0} - f^t. \tag{2.63}$$

The transformation function constraining the evolution of the martensitic volume fraction (2.21) can be written as

$$\Phi^t = \begin{cases} \Phi^t_{fwd} = 2(1-D)(\tau+\beta)\Lambda^t(\tau) \\ \qquad + 4(1+\nu)\tau^2\left(\frac{1}{E_m} - \frac{1}{E_a}\right) \qquad ;\dot{\xi} > 0, \\ \qquad + \rho^m\tilde{s_0}T - \rho^m\tilde{u_0} - f^t_{fwd} - Y_0 \\ \Phi^t_{rev} = -2(1+D)(\tau+\beta)\Lambda^t(\tau) \\ \qquad - 4(1+\nu)\tau^2\left(\frac{1}{E_m} - \frac{1}{E_a}\right) \qquad ;\dot{\xi} < 0, \\ \qquad - \rho^m\tilde{s_0}T + \rho^m\tilde{u_0} + f^t_{rev} - Y_0 \end{cases} \tag{2.64}$$

where D is a model parameter that captures the stress dependency of the critical thermodynamical force. The parameters $\tilde{u_0}$, Y_0, a_1, a_2, and a_3 can be found as

$$a_1 = \rho\tilde{s_0}\left(M_f - M_s\right), \tag{2.65a}$$

$$a_2 = \rho\tilde{s_0}\left(A_s - A_f\right), \tag{2.65b}$$

$$a_3 = -\frac{a1}{4}\left(1 + \frac{1}{n_1+1} - \frac{1}{n_2+1}\right) + \frac{a2}{4}\left(1 + \frac{1}{n_3+1} - \frac{1}{n_4+1}\right), \tag{2.65c}$$

$$\rho\tilde{u_0} = \frac{\rho\tilde{s_0}}{2}\left(M_s + A_f\right) + 2\beta\Lambda^t\left(0\right), \tag{2.65d}$$

$$Y_0 = \frac{\rho\tilde{s_0}}{2}\left(M_s - A_f\right) - a_3 - 2\beta D\Lambda^t\left(0\right), \tag{2.65e}$$

with

$$D = -\frac{\left(C_a - C_m\right)\left[\Lambda^t\left(\tau^*\right) + \left(\tau^* + \beta\right)\frac{\partial\Lambda^t(\tau^*)}{\partial\tau} + 4\left(1+\nu\right)\tau^*\left(\frac{1}{E_m} - \frac{1}{E_a}\right)\right]}{\left(C_a + C_m\right)\left[\Lambda^t\left(\tau^*\right) + \left(\tau^* + \beta\right)\frac{\partial\Lambda^t(\tau^*)}{\partial\tau}\right]}, \tag{2.66a}$$

$$\rho\tilde{s_0} = -\frac{4C_aC_m\left[\Lambda^t\left(\tau^*\right) + \left(\tau^* + \beta\right)\frac{\partial\Lambda^t(\tau^*)}{\partial\tau} + 4\left(1+\nu\right)\tau^*\left(\frac{1}{E_m} - \frac{1}{E_a}\right)\right]}{C_a + C_m}, \tag{2.66b}$$

where τ^* is the calibration stress. With this transformation function for the SMA tube under pure torsion known, equations 2.26 and 2.61b can be combined to get

$$\frac{1}{2}\rho J_{e0}\cdot J_{e0}^* - \nabla\cdot q = \left(-\Pi\left(\tau, T, \xi\right) + \rho^m\tilde{s_0}T\right)\dot{\xi} + \rho^m c\dot{T}, \tag{2.67}$$

where terms containing $\tilde{c}$ and $\tilde{\alpha}$ have been neglected as is common in SMA constitutive modeling. The shear stress rate $\dot{\tau}$ has also been neglected since it is assumed in this ODE solution that τ is time independent (i.e. the applied stress is either constant or a function of rotation due to transformation). The eddy current density J_{e0} is taken to be of a single component as was done with the magnetic and electric fields. Equation 2.67 can be rewritten by noting that $\dot{\xi}$ is only nonzero when the

SMA is transforming and recalling that $\dot{\xi}\Phi^t = 0$ giving

$$\frac{1}{2}\rho J_{e0} \cdot J_{e0}^* - \nabla \cdot q = \left(\mp Y^t + \rho^m \tilde{s_0} T\right)\dot{\xi} + \rho^m c\dot{T}, \tag{2.68}$$

where $Y^t = Y_0 + 2\left(\tau + \beta\right) D\Lambda^t\left(\tau\right)$ and the notation of "$\mp$" has been introduced with the upper sign used to indicate forward transformation and the lower to indicate reverse. Finally, it is noted that the only heat sources and sinks are due to induction heating and convective terms so equation 2.68 can be written in its final form as

$$\frac{\rho}{2} J_{e0} \cdot J_{e0}^* - h\frac{A}{V}\left(T - T_\infty\right) = \left(\mp Y^t + \rho^m \tilde{s_0} T\right)\dot{\xi} + \rho^m c\dot{T}, \tag{2.69}$$

where A and V are the area and volume of the SMA tube being modeled, not area and volume of the assumed thin walled tube.

2.5.3 ODE Solution Implementation

The ODE solution is implemented in Matlab using the return mapping algorithm as described in [46]. The inputs to this model are the initial temperature, initial martensite volume fraction, SMA tube dimensions, electric current, frequency, number of coil turns, and the heating/cooling times. The ODE solution uses a Gauss-Seidel time marching scheme shown in figure 2.4. This process has been successfully used in other coupled SMA based problems [5, 60]. In this scheme the appropriate initial conditions are passed to both the electromagnetic and thermo-mechanical algorithms. The temperature and phase are then given to the electromagnetic problem to evolve the resistivity and solve for a new Joule heating power, which is then passed back to the thermal problem. The process is continued in this manner for the duration of the heating and cooling process.

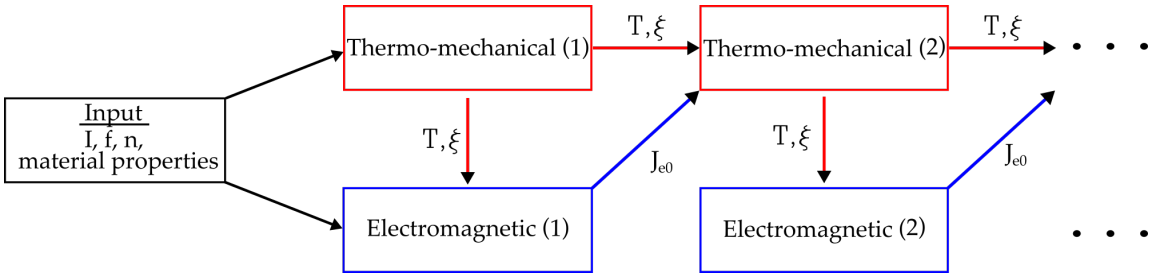

Figure 2.4: Gauss-Seidel time marching scheme used to couple the electromagnetic behavior to the thermo-mechanical behavior in the ODE solution.

3. MATERIAL CONSTANT DETERMINATION

Calibration of the SMA material properties is required to ensure the accuracy of both the FE model and ODE solution. The calibration was performed in two stages: the electromagnetic phase and the thermo-mechanical constitutive phase.

3.1 Electromagnetic Constants

As discussed in section 2, the only material properties required to model the electromagnetic behavior of the SMA are the electrical resistivity and magnetic permeability. Experimental measurements showed that the relative permeability of NiTi is approximately 1.002 in either phase, which is also observed in the literature [11]. The experiments showed that the SMA resistivity is 76 $\mu\Omega$-cm in austenite and 82 $\mu\Omega$-cm in martensite. In the ODE solution, this value is evolved with transformation and with temperature. Experiments were not performed to determine the temperature dependence of the resistivity so it is assumed that it evolves in the same matter as a NiTi wire [59, 19]. Specifically, the resistivity is evolved according to

$$\rho\left(T,\xi\right)=\rho_a\left(T\right)+\xi\left(\rho_m\left(T\right)-\rho_a\left(T\right)\right), \tag{3.1}$$

where $\rho_\zeta\left(T,\xi\right)=\rho_\zeta+\left(d\rho_\zeta/dT\right)T$. The temperature dependence $\left(d\rho_\zeta/dT\right)$ was taken to be constant and equal to 0.1 $\mu\Omega$-cm/K [19] in both phases.

For the sequentially coupled (feedforward) FEA approach, it is not feasible to change the resistivity with phase changes. Therefore, a single constant resistivity of 80 $\mu\Omega$-cm was chosen. This value was chosen based on the results of a finite element analysis on an SMA torque tube shown in figure 3.1. The tube in each case was subject to identical conditions with the exception that the resistivity was varied from

the martensitic value to an intermediate value (used in the final FEA implementation) to the austenitic value. The ratio of the Joule heating rate at the outer surface

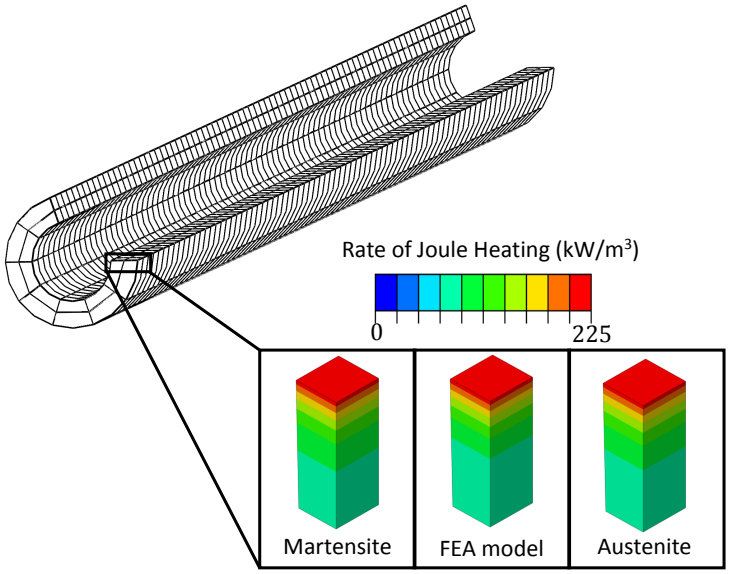

Figure 3.1: Effect on Joule heating due to a change in resisitivity in the FE model. The resistivity was varied from the martensitic value to an intermediate value (used in the final FEA implementation) to the austenitic value.

to the inner surface was used to determine the effect of a changing resistivity. The differences of the ratios were as follows: 8.7% difference between martensite and austenite values, 6.0% difference between the intermediate and austenitic values, and 2.85% difference between the intermediate and martensitic values. These results demonstrate that the assumption of constant resistivity is sufficiently accurate for the FE model.

3.2 Thermomechanical Constants

The constitutive model was calibrated using experiments performed on a homogeneous, prismatic tube with length L of 8 in. (203 mm) with outer d_e and inner d_i

diameters of 0.375 in. (9.525 mm) and 0.225 in. (5.715 mm), respectively. To determine the material constants, the tube was subjected to thermal cycles under different constant torques. The tube is fixed at one end (zero displacement) and has an applied twisting moment at the opposite end (applied traction). The lateral surfaces of the tube are traction free. The temperature is spatially uniform and varies from below the martentsite finish temperature to above the austenite finish temperature. The torque T was measured in the experiment and then converted to shear stress to be compatible with the FEA outputs by

$$\sigma_{23} = \sigma_{32} = \tau = \frac{T d_e}{2J} \tag{3.2}$$

where τ is the shear stress at the outer surface of the tube, and J is the second moment of area given for hollow tubes as $\frac{\pi}{32}\left[d_e^4 - d_i^4\right]$ [7]. The normalized rotation-temperature curves generated by this experiment following the conversion from torque to outer surface shear stress are shown in figure 3.2, which is used for the remainder of the thermo-mechanical material constant determination. The normalized rotation is the rotation measured multiplied by the ratio $d_e/(2L)$. The temperature in the experiment was measured by a thermocouple placed on the outer surface of the tube at the mid-length. During these experiments, induction heating was used to transform the SMA tube.[1]

The first step in determining the material constants is to consider the thermoelastic response, which provides the austenite and martensite elastic moduli, Poisson ratios, and thermal expansion coefficients. The austenite and martensite Poisson ratios are assumed to be equal and constant as is common in macro-scale SMA

[1]The frequency in the induction system was such that the thermal gradients in throughout the tube were small and when the results are compared to more conventional and thermally uniform conductive heating, there is no significant difference.

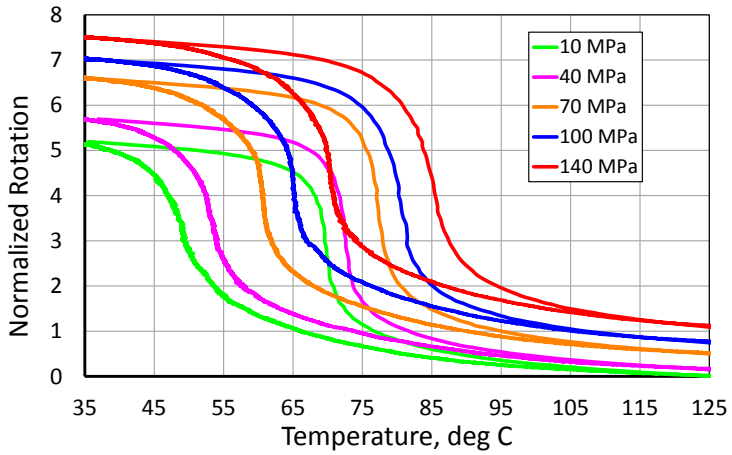

Figure 3.2: Experimental normalized rotation-temperature diagram for torsional loading of a NiTi tube ($d_e = 9.525\,\text{mm}$, $d_i = 5.715\,\text{mm}$) corresponding to approximately 1, 5, 9, 13, 18.5 N-m of applied torque. The normalized rotation is the rotation measured multiplied by the ratio $d_e/(2L)$.

modeling. The thermal expansion response is neglected as it does not contribute to shear stress. To determine the elastic modulii, the shear stress and normalized rotation were read from figure 3.2 for each loading when the tube is completely austenite and martensite and then plotted to create what has been referred to as the dynamic modulus [51], shown in figure 3.3. Assuming a perfectly trained material, the strain in austenite is purely elastic so that the shear modulus G can easily be measured as the slope of the fit to the austenite line in figure 3.3. The modulus in martensite depends on the amount of transformation strain the SMA has developed. However, for this highly trained tube the behavior is close to linear so that the martensite shear modulus can be approximated in the same manner as the austenite modulus. The shear modulii for the tube as measured from figure 3.3 are then used to calculated to the elastic modulii by $E = 2(1+\nu)G$.

The transformation constants are divided into three categories: the phase diagram parameters, the transformation strain parameters, and the smooth hardening

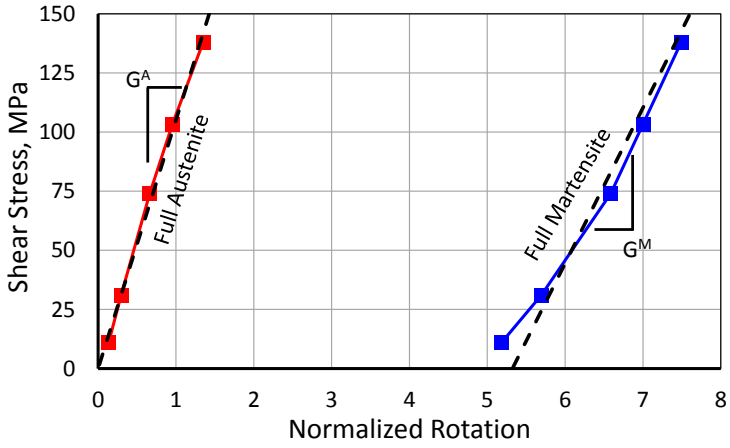

Figure 3.3: SMA tube dynamic modulus measurements correspond to figure 3.2 with linear fit.

parameters. The smooth hardening parameters, $n_1 \ldots n_4$, can be tuned in the range $0 < n_i \leq 1$ to approximate "smoothness" of the transformation hysteresis. The phase diagram parameters that must be determined are the martensite and austenite start and finish temperatures (M_s, M_f, A_s, A_f) and martensite and austenite stress influence coefficients (C^M, C^A) as shown in [48]. The transformation strain parameters include the maximum transformation strain (H_{Max}), the back stress tensor $(\boldsymbol{\beta})$, and k^t. For the case of a torque tube, $\boldsymbol{\beta}$ is taken to be a single non-zero component such that $\beta_{23} = \beta$ all others zero and the 2-3 (θ-Z) direction corresponds to torsion about the longitudinal axis. This is the same assumption used in the derivation of the ODE solution.

A first-order approximation was made for the phase diagram properties simply by inspection of figure 3.2, and the initial smooth hardening and transformation strain parameters were found in the literature [50]. Finding the material constants in this manner generally gives a model that is approximate but does not capture the full behavior of the SMA. To refine the parameters, a finite element model of the test

was constructed, as shown in figure 3.4. In this model the geometry, loading, and boundary conditions match the test setup so that only the transformation constants are varied to match the experiment data. The model consists of 1600 three dimensional quadratic reduced integration brick elements (Abaqus designation C3D20R). The FE model is chosen over the ODE solution to calibrate the material constants for multiple reasons. The primary reason for this choice is that the tube used in the experiment is *not* thin walled and thus the ODE solution, which assumes a thin walled tube, will not be as accurate as the FE model. Following the calibration a comparison of the ODE solution, FE model, and experiment will be made using the calibrated parameters to determine how good the assumption of a thin walled tube is in the ODE solution.

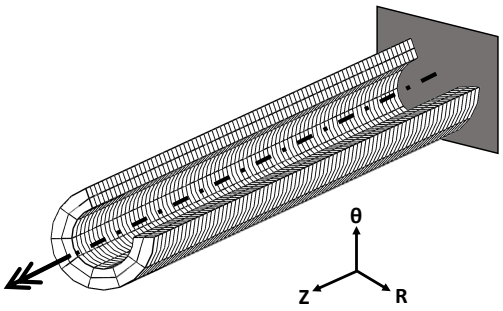

Figure 3.4: Finite element model created to determine the SMA transformation constants. One quarter of the model is cutaway for detail.

While an optimization with the FE model would be the most accurate way to determine the constants by minimizing the error between the FEA and experiment, the process to set up an optimization is not trivial and this work is intended to focus more on the thermal behavior of the SMA rather than the transformation

behavior. The final result of the approximated calibration is shown in figure 3.5 where the experiment is compared to the ODE solution and calibrated FE model. The calibrated parameters from the FEA are used in the ODE solution without modification.

As can be seen from figure 3.5, the calibrated FE model and ODE solution agree well with each other and the experiment. The agreement between the FE model and ODE solution indicates that the assumption of a thin walled tube to analyze the SMA may not significantly effect the results. However, this calibration does not consider inductive heating, which is a strong function of radius and workpiece dimensions so some error in the time history may be introduced when this is considered later. The result of the calibrations are summarized in table 3.1. These parameters are used when modeling the SMA tube. No experiments were performed to calibrate the SMA beam material properties as no associated experimental study of inductively heated SMA beams has been performed. Instead, properties were taken directly from [32]. The beam properties are also summarized in table 3.1.

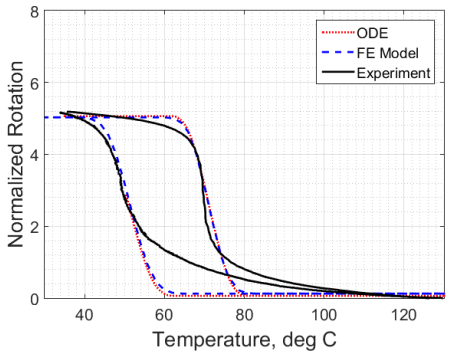

(a) 10 MPa experiment and model comparison.

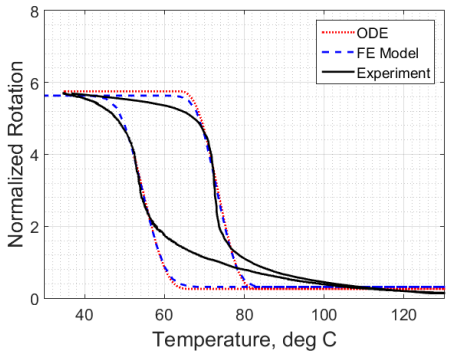

(b) 40 MPa experiment and model comparison.

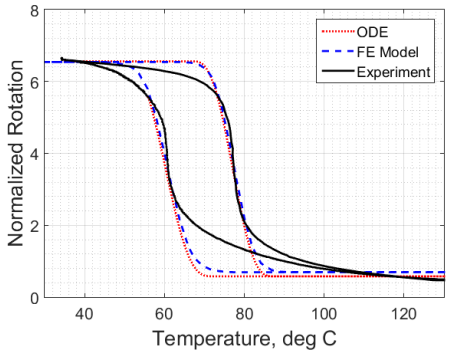

(c) 70 MPa experiment and model comparison.

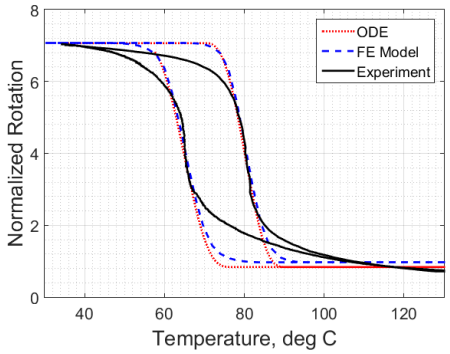

(d) 100 MPa experiment and model comparison.

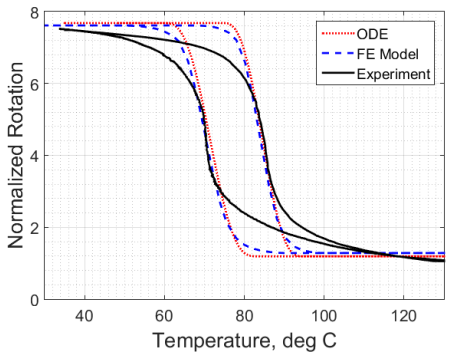

(e) 140 MPa experiment and model comparison.

Figure 3.5: SMA calibration experiment compared to the ODE solution and calibrated FE model. The calibrated parameters from the FEA are used in the ODE solution without modification.

Table 3.1: SMA electromagnetic and constitutive material parameters.

Property	**Tube**	**Beam**[†]
(Electromagnetic Parameters)		
μ_r	1.002	1.002
ρ ($\mu\Omega$-cm)	80	80
(Heat Transfer Parameters)		
γ (kg/m^3)	6450	6450
c (J/kg/K)	400 (850[§])	400
k (W/m/K)	10	10
(Thermoelastic Parameters)		
E^A (GPa)	27.98[‡]	90.0
E^M (GPa)	17.49[‡]	63.0
$\nu^M = \nu^A$	0.33	0.33
$\alpha^M = \alpha^A$ (/K)	0.00	10×10^{-6}
(Phase Diagram Parameters)		
M_s, M_f (K)	335 , 311	295 , 280
A_s, A_f (K)	333 , 354	353 , 362
C^M, C^A (MPa/K)	5.5 , 7.9	5 , 10
(Transformation Parameters)		
H_{Max} (%)	3.35	6.0
k^t (/MPa)	0.0172	0.00752
β (MPa)	58	0.0
(Smooth Hardening Parameters)		
$n_{1,2,3,4}$	0.3	0.35

[†] After [32], where applicable.

[‡] Calibrated from torsion testing.

[§] Used only for the ODE solution based on NiTi wires.

4. RESULTS

4.1 SMA Torque Tube

The tube in this study is the same that is described in chapter 3 and is shown with an idealized (i.e. homogenized) coil model in figure 4.1. The analysis of the

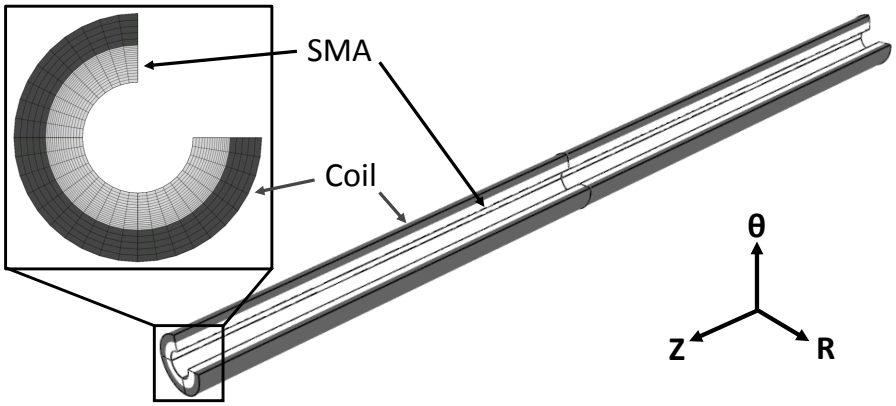

Figure 4.1: Electromagnetic FE model of the SMA torque tube with the vacuum domain omitted. One quarter of the model is cut away for visualization. The mesh through the thickness is shown enlarged for detail.

tube in the FE model is completed in two stages as previously described. For the electromagnetic analysis the entire domain, including the coil and tube, is meshed with 50190 electromagnetic linear hexahedral electromagnetic elements (Abaqus designation EMC3D8); the mesh is concentrated through the thickness of the SMA tube where gradients are highest and of most interest. In the thermo-mechanical portion of the analysis only the tube is modeled using 4370 linear hexahedral temperature-displacement elements with reduced integration (Abaqus designation C3D8RT). The thermo-mechanical model is similar to that shown in figure 3.4 with a more refined

mesh. The refined mesh accommodates mapping of the Joule heating field from the electromagnetic result to each element in the thermo-mechanical model and helps to better capture thermal gradients.

Two experimental tests of this tube are simulated and compared to the FE model and ODE solution. The first is an input study where the power into the induction coil is varied to determine how the developed models compares to various inputs. The second study is a high rate actuation test to verify the behavior of the models at a relatively small time scale. A final test of the FE model only is simulated and not completed experimentally, which shows the effects of a changing frequency on the variation of temperature, shear stress, and martensite volume fraction through the tubes wall thickness.

4.1.1 Power Variation Study

In the first study, the input power to the experimental induction system is varied and the temperature at the middle of the tube on the outer surface is measured. The power is varied by maintaining a constant frequency and varying the coil current across three levels. The three input RMS coil currents are 49.9 A, 45.3 A, and 21.4 A at a frequency of 55 kHz, which correspond to input power levels of 1150 W, 840 W, and 225 W respectively. By treating the induction system as a transformer, the impedance can be found. This allows a real power in the coil to be found. The real coil power is the power which contributes to the heating of the SMA and coil. It is assumed that the coil is not being heated so that all of the power is transferred into the SMA. The real coil powers produced were found to be 488 W, 417 W, and 135 W and correspond to input powers of 1150 W, 840 W, and 225 W respectively. The real coil power, which assumed to be completely transferred to the SMA body, agrees well with the power found through the FE model. The temperature is measured by a

non-conductive type K thermocouple. The study uses a 10 AWG copper magnet wire wrapped tightly around the SMA tube. There is no active cooling in this scenario to minimize the number of possible variables in the experiment. In this study only the heating of the tube is modeled since cooling is accomplished by free convection over a long time relative to heating. The torque in all 3 power measurements was held constant at 21 N-m. The results of the experiment and models are shown in figure 4.2. The FE model agrees well with the experimentally measured temperature within 15% at all times. The largest discrepancies between the FEA and the experiment are due to the effects of latent heat, which are not considered in the FE model. The addition of the effects of latent heat in the ODE solution allow for the significant deviations from linearity to be captured, but in general the ODE solution overestimates the rate of heating in the SMA body. The overestimate is likely due to the simplifying assumptions in the ODE solution. However if experiments are completed on the SMA tube far above and below the transformation temperatures, the thermal behavior (more precisely, the specific heat) in the absence of transformation can be characterized and calibrated to in the ODE solution. This could result in a model that is able to better capture the behavior in time of the SMA thus making the ODE solution ideal for optimization and analysis applications.

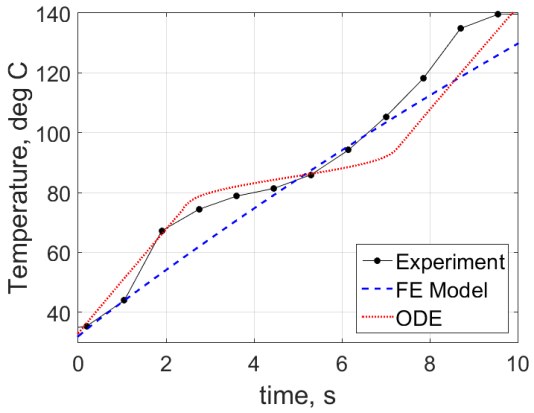

(a) 1150 W induction heating power measurement.

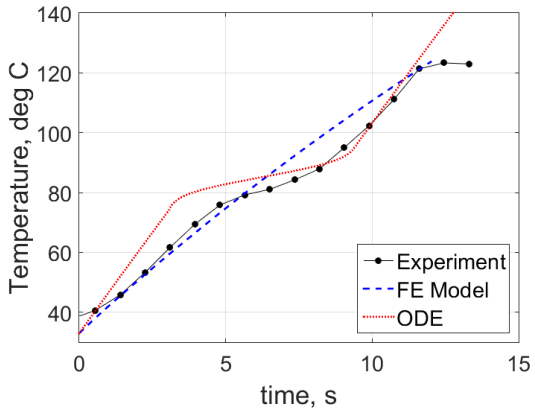

(b) 840 W induction heating power measurement.

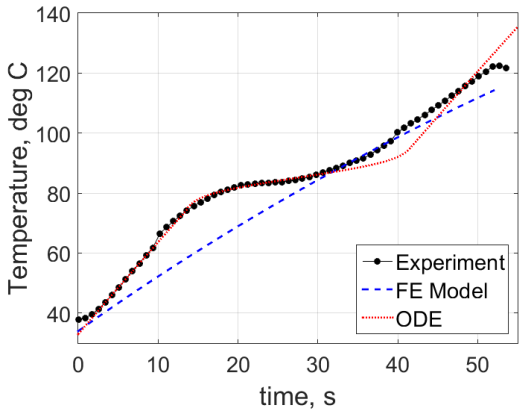

(c) 225 W induction heating power measurement.

Figure 4.2: Power measurement study results. The highest heating rates correspond to the highest input power.

In section 1.2, it was noted that resistive heating large SMA components like torque tubes is limited by current. To show this qualitatively, the real coil power measurements in the previous experiments are used in a simple resistive heating calculation given as

$$P = I^2 \rho \frac{L}{A}, \tag{4.1}$$

where P is the power, I is the DC current, ρ is the resistivity (taken to be $80\,\mu\Omega$-cm), L is the length, and A is the cross sectional area of the tube ($\frac{\pi}{4}\left[d_e^2 - d_i^2\right]$). For the particular tube implemented this can be reduced to $P = 3.56 \cdot 10^{-3} I^2$. The DC current I needed to generate an equivalent power to the induction system can now be solved for 488 W, 417 W, and 135 W as 370 A, 342 A, and 195 A respectively. These currents are significantly higher than current of 49.9 A, 45.3 A, and 21.4 A used in the induction system, demonstrating why resistive heating can be difficult to achieve in large pieces.

4.1.2 High Rate Actuation Study

With the FE model able to demonstrate that it has the capability to match experimental results well and the ODE solution able to produce comparable results, a second study was complete to achieve high rate actuation in the SMA tube. In this second study, the high rate heating was achieved my changing from a 10 AWG coil to a smaller 14 AWG coil to increase the current density. In the induction coil an RMS current of 33 A and voltage 31.5 V were applied at 49.1 kHz. The applied torque again remained constant at 21 N-m. To achieve high rate cooling, active cooling was implemented by flowing a mixture of 90% water and 10% ethylene glycol at a volumetric flow rate of 1.2 gal/min ($75\,\mathrm{cm}^3/\mathrm{s}$) through the tube. During heating this mixture was stationary in the tube. A diagram of this cooling setup is shown in figure 4.3. The extra components to accommodate coolant flow were not included in the FE model and only the active portion of the tube is considered. The thermal effect of the flow was simulated using a convection boundary condition in both the ODE solution and FE model.

The magnetic and electric fields induced in the high rate actuation study as simulated by the FE model are shown in figure 4.4, where the end portion of the tube

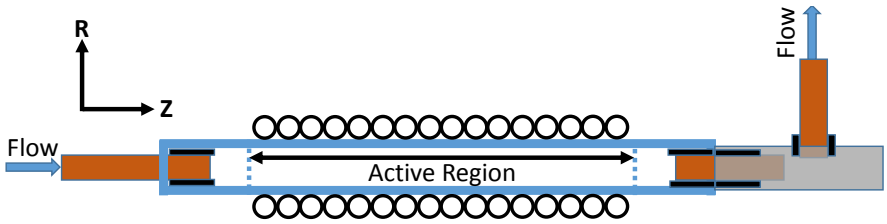

Figure 4.3: SMA tube diagram for coolant flow with sample induction coil shown.

is shown in particular as the fields become uniform away from the ends. The ability to visualize these fields both inside and outside of the SMA helps in understanding possible consequence arising from the generation of a free magnetic or electric field in a system that involves other electronics.

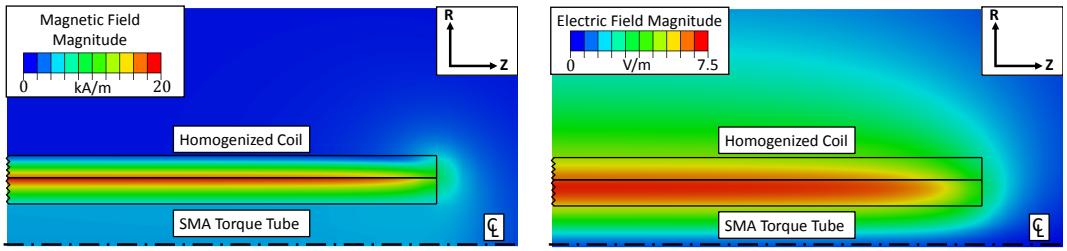

(a) Magnetic field magnitude (b) Electric field magnitude

Figure 4.4: Induced time harmonic electromagnetic field magnitudes in the SMA and surrounding domain for the high rate actuation study as simulated by the FE model.

The rate of Joule heating induced by eddy currents in the tube is shown in figure 4.5 and is a result of the electromagnetic fields from figure 4.4. All fields show a distinct end effect which lowers the overall heating rate of the system; in the case shown the effect on the overall heating rate is small.

In both the ODE solution and FE model, a free convection condition boundary condition was used to model the stationary water during heating. The FEA result

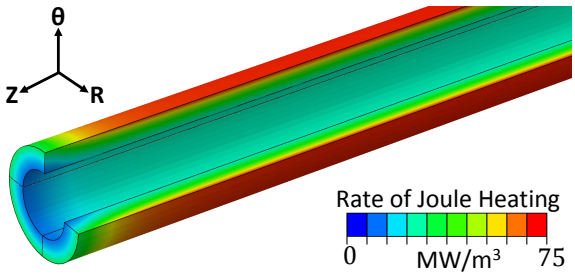

Figure 4.5: Rate of Joule heating induced in the SMA due to the time harmonic electromagnetic fields of figure 4.4 during the high rate actuation study.

of this was compared to an adiabatic case in figure 4.6 so the effects of the stationary water in the tube during heating are made more apparent. During cooling, a convection coefficient must be calculated from analytical solutions or use of a fluid dynamics analysis. The latter is beyond the scope of this work. Rather, an effective convection coefficient was calculated. The result of this calculation as simulate by the FE model is shown in figure 4.6 and further calculation details are discussed in appendix A.

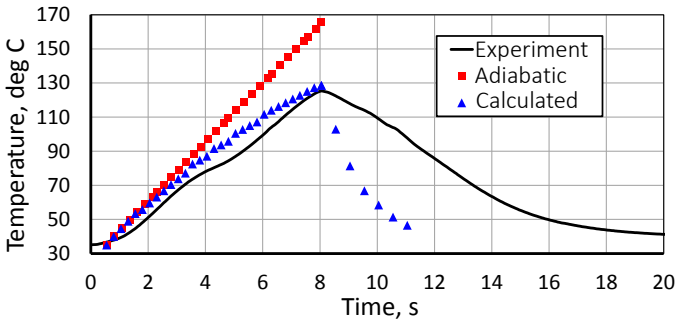

Figure 4.6: Temperature response of the SMA tube in the high rate actuation study using the FE model with calculated convection coefficient. The experiment data is compared to adiabatic conditions and calculated convection conditions.

The result of the calculated convection coefficient is not in good agreement with

the experiment so a parametric study was completed in the FE model to determine a convection coefficient that could describe the cooling process. The result of this study is shown in figure 4.7 and described in more detail in appendix A. Due to the simplifying assumptions used in the ODE solution, the convection coefficient calculated for the FE model is not valid in the ODE solution. The same method of implementing a parametric study to determine an effective convection coefficient was used for the ODE solution with the exception that a constant temperature was used to find the convection coefficient. The detailed output of this study is omitted and the end result is shown in figure 4.7.

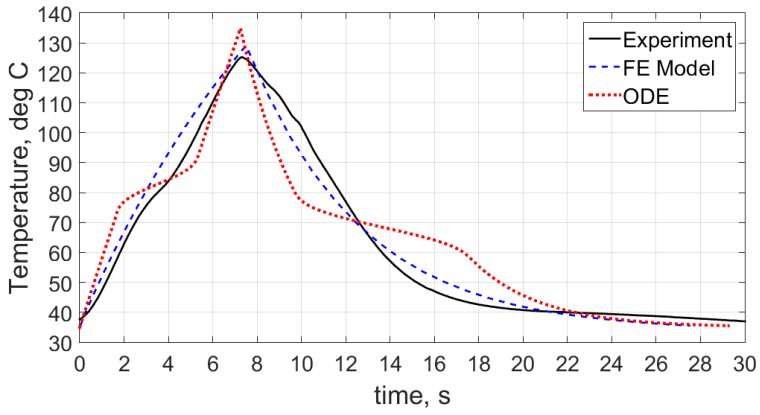

Figure 4.7: High rate actuation experiment results following the application of a parametric study to determine a convection coefficient.

From figure 4.7, it can be seen that the FE model compares well to the experiment in time. The ODE solution, in this study, predicts the maximum temperature in time well. The only significant deviations from the experiment occur due to the consideration of latent heat which is not noticeable in this particular experiment. To

examine the source of this error, the normalized rotation developed over time in the experiment is compared to the FE model and ODE solution in figure 4.8a.

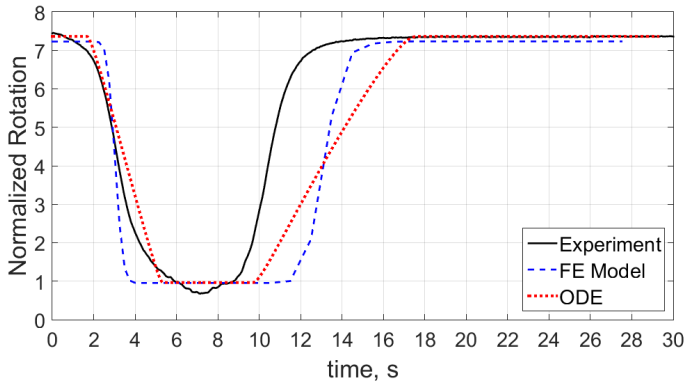

(a) Normalized rotation developed in time in the SMA tube experiment compared to the ODE solution.

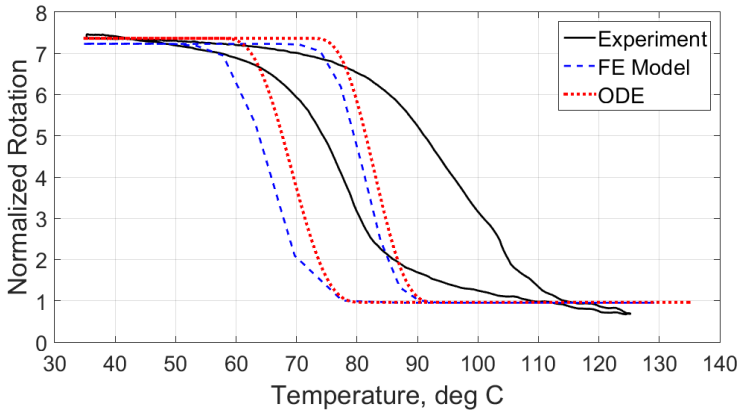

(b) Normalized rotation developed with temperature in the SMA tube experiment compared to the ODE solution.

Figure 4.8: Comparison of normalized rotation developed in time and temperature between the ODE solution and experiment.

There is a large discrepancy at the time when transformation is finished between

the experiment, FE model, and ODE solution. Furthermore there is a discrepancy in the normalized rotation-temperature behavior when compared to the experiment. Recall that that SMA tube used in this study is the same that was calibrated to in section 3, therefore the normalized rotation-temperature behavior should be accurate however this is not the case. The FE model and ODE solution agree as expected based on the previous calibration. It is likely that the effects of active cooling and the large gradients due to induction heating cause an unexpected structural behavior that is not being captured by either model.

4.1.3 Frequency Variation Effects

In the two previous studies, the FE model has proven to be accurate during the heating of the tube and with some manipulation is able to analyze cooling also. The FE model is now used to analyze the effects of changing the frequency, and therefor Joule heating distribution, in the SMA tube. The effects of increasing the frequency are not able to be captured in the ODE solution as the radial dependence has been neglected. As the frequency is increased the corresponding skin depth is decreased meaning that larger gradients will exist in the thick walled tube being modeled. These stronger gradients are not able to be captured in the ODE solution due to the assumption that the radial gradients are small enough to be neglected. In this study, the tube is subject to a constant 13 N-m torque then heated for 5 s using a 14 AWG coil with an RMS current of 35 A. The tube is cooled for 20 s using the same active cooling scenario demonstrated in the previous study. The purpose of this study is to visualize the effects of a changing induction frequency on the radial distributions of temperature, martensite volume fraction, and shear stress. It is important to note that this is a purely numerical study and no experiments have been performed.

The radial temperature distributions in time are shown in figure 4.9 with the cor-

responding martensite volume fractions and shear stresses shown in figures 4.10 and 4.11 respectively. In these figures the normalized radial position corresponds to 0 at the inner surface of the tube and 1 at the outer surface. Due to the skin effect of 1.1, the radial temperature gradient is more pronounced at higher frequencies. The higher frequencies also produce a higher overall temperature in the tube than do lower frequencies at the same current. Recall from 2.46 that Joule heating is quadratic with the eddy currents magnitude, which is a sinusoidal function of frequency.

This temperature variation with frequency is then manifested in the martensite volume fraction during heating as the higher frequencies lead to earlier transformation during heating and delayed transformation during cooling. The skin depth effect at high frequencies also causes a strong gradient in the evolution of martensite through the radius of the tube. For lower frequencies, the radial temperature gradient is small and the shear stress before transformation varies approximately linearly in the radial direction, as expected in tubes. Therefore, the martensite evolves approximately linearly in the radial direction. However, for higher frequencies, the higher radial temperature gradients cause a highly nonlinear behavior that can, to some extent, be controlled by the magnitude and frequency of the coil current. This controlability provides new possibilities for optimizing the actuation systems for particular applications (e.g. increasing fatigue life, optimizing training procedures, etc.). Note in particular the case of 1000 kHz, where a θ-Z shear stress increase of 70 MPa over the nominal as loaded stress of 88 MPa is observed. In addition to the large θ-Z shear stress gradient at 1000 kHz, there is also an observed increase in R-θ shear stress gradient. The difference in the maximum and minimum R-θ shear stress changes from approximately 1 MPa in the low frequency cases to about 5 MPa in the 1000 kHz case.

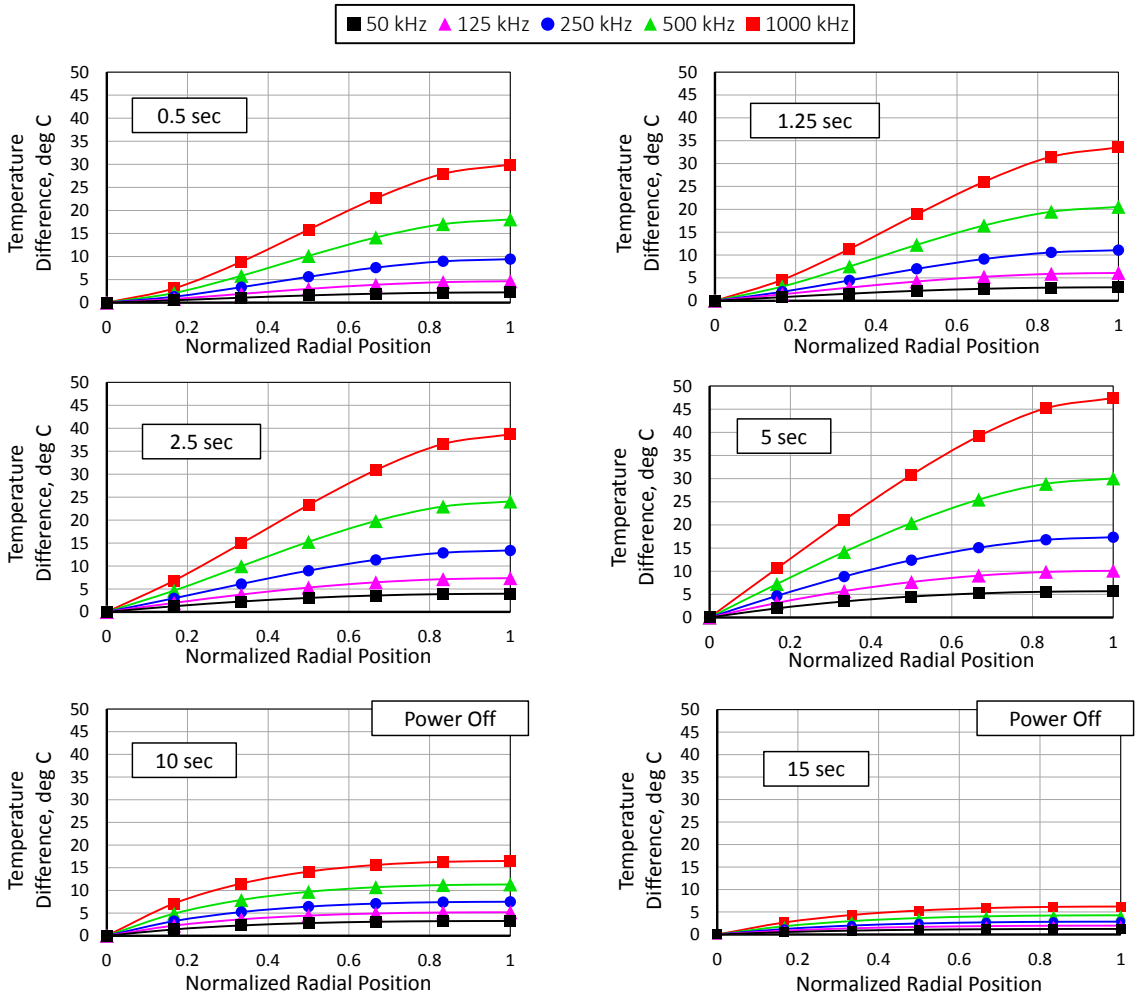

Figure 4.9: Temperature distribution at varying frequencies and a constant loading. The normalized radial position corresponds 0 at the inner surface of the tube and 1 at the outer surface. The temperature difference is measured relative to the temperature at the inner surface. Heating for 5 seconds using a 14 AWG coil with an RMS current of 35 A followed by active flow cooling using the results of the high rate actuation study.

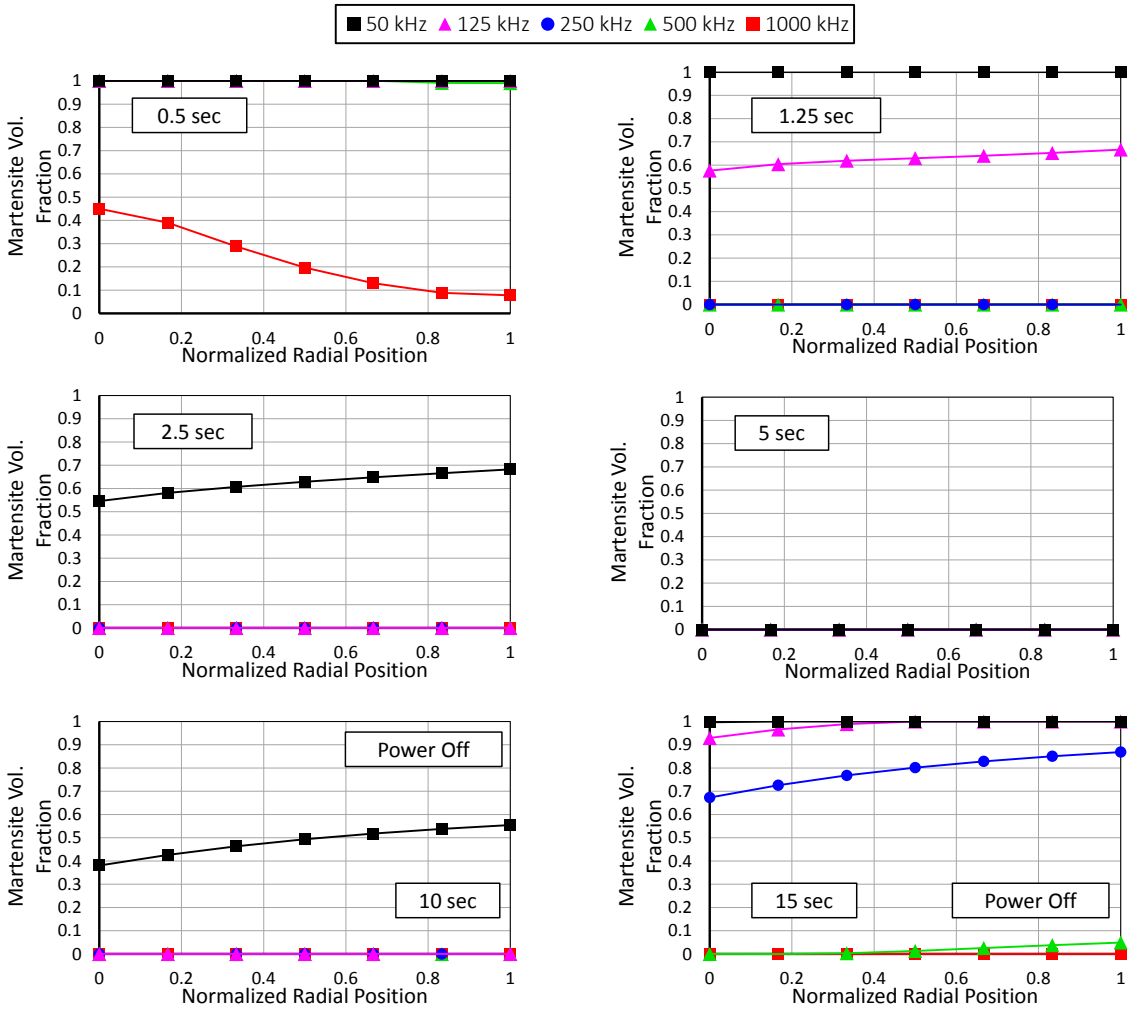

Figure 4.10: Martensite volume fraction profile through the tube thickness at various frequencies and a constant loading. Heating for 5 seconds using a 14 AWG coil with an RMS current of 35 A followed by active flow cooling using the results of the high rate actuation study.

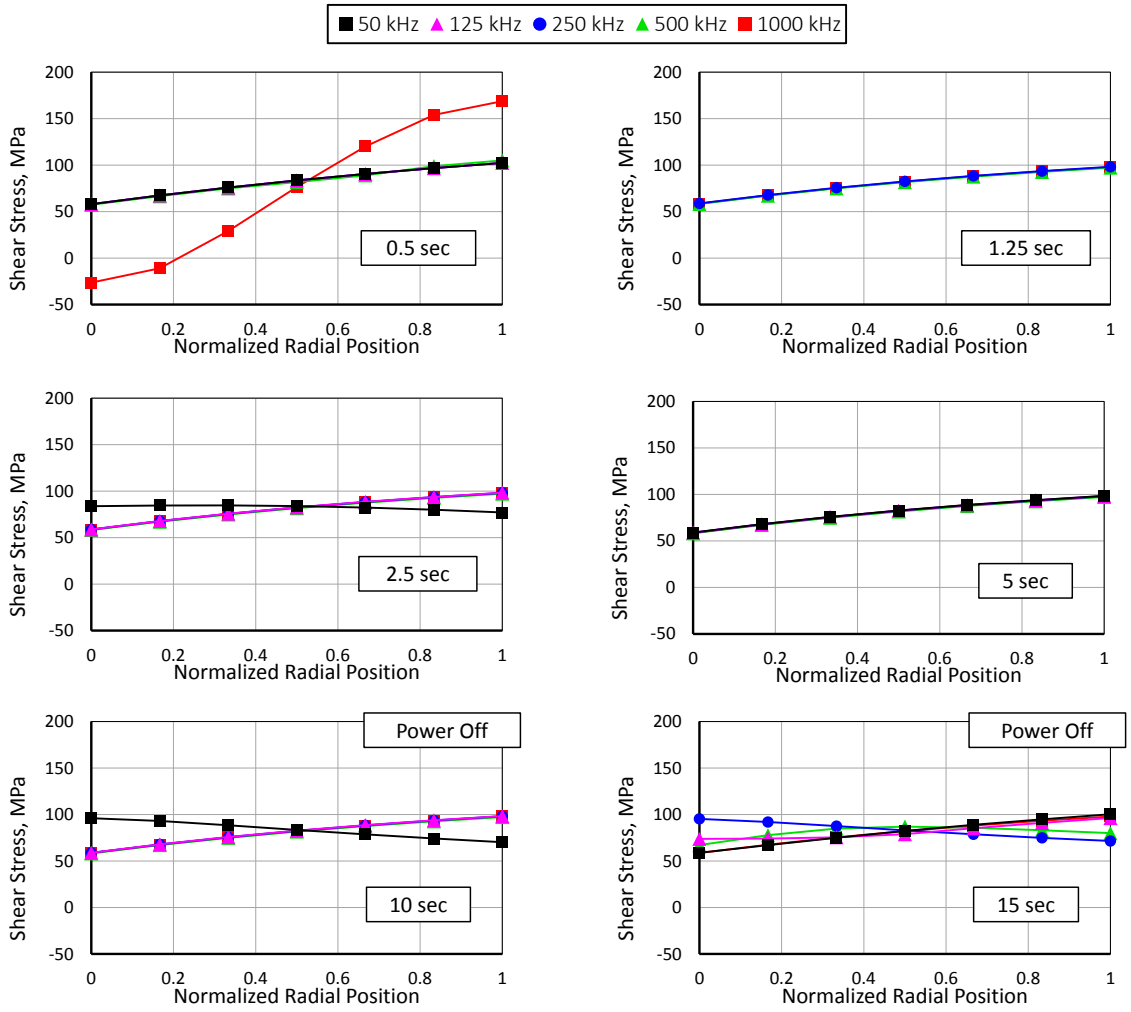

Figure 4.11: θ-Z Shear stress profile through the tube thickness at various frequencies and a constant loading. Heating for 5 seconds using a 14 AWG coil with an RMS current of 35 A followed by active flow cooling using the results of the high rate actuation study.

The sum of all of these frequency induced effects demonstrates why it is necessary for both an FE model and ODE solution to exist. For cases where a high frequency is used and the radial distribution of Joule heating power through the SMA contains

strong gradients, an FE model is the only tool able to capture the behavior. In cases where the skin depth and thickness are approximately the same, as has been the case in the prior experiments, the radial gradients of Joule heating power are much smaller due to the lower frequency. This allows the Joule heating power to be approximated as constant without a drastic loss in accuracy and added benefit of having a substantially reduced computational time.

4.2 SMA Bending Beam

An SMA beam heated by a planar induction coil was likewise simulated only by the FE model and was not experimentally studied. A planar coil is the configuration used in induction cook tops [34]. The RMS coil current and frequency considered are 40 A and 55 kHz, respectively. The SMA beam has length of 5 in. (127 mm), a width of 1.5 in. (38.0 mm), and a thickness of 0.2 in. (5.1 mm). The outer diameter of the coil is equal to the width of the SMA beam, with 12 turns of 20 AWG copper wire. The homogenized coil on the SMA beam is shown in figure 4.12a and, as before, is taken to be a homogenized current sheet rather than modeling the individual coil turns. The coil is placed at the fixed end of the beam. The free end of the beam has a constant force of 75 N applied orthogonal to the beam axis and in the direction of the beam short dimension.

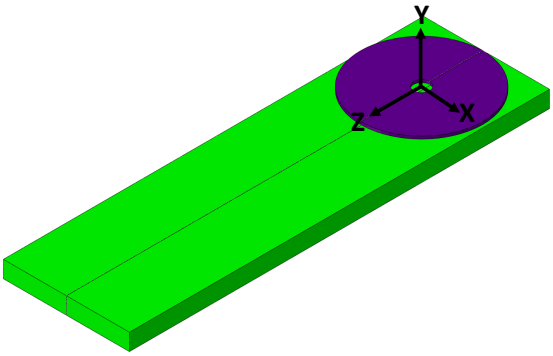

(a) SMA beam with circular coil geometry.

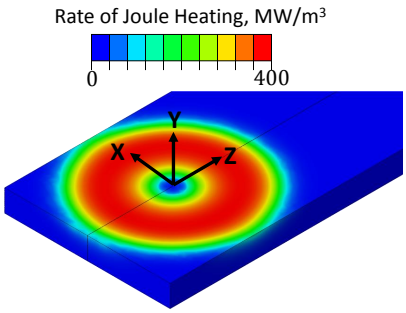

(b) Rate of Joule heating produced in the SMA by the circular coil.

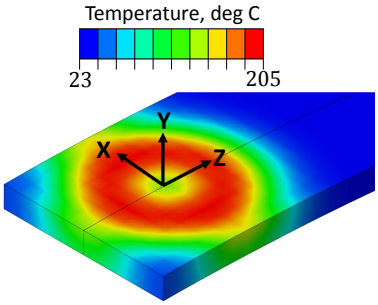

(c) Corresponding temperature profile in the SMA beam.

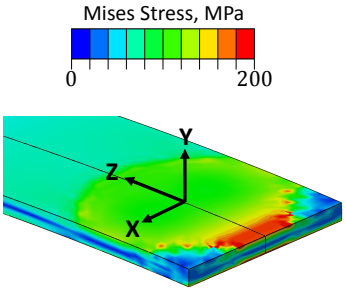

(d) Mises stress profile in the SMA beam due to a constant force of 75 N applied orthogonal to the beam axis and in the direction of the beam short dimension.

Figure 4.12: Homogenized 12 turn 20 AWG circular coil on an SMA beam. The beam is heated for 5 s using an RMS current of 40 A at 55 kHz

As another example, a rectangular planar coil with the same input current, width, and 20 AWG wire as the circular coil is considered, where the length is 2 in. (50.8 mm) and only 4 turns of wire are considered as shown in figure 4.13.

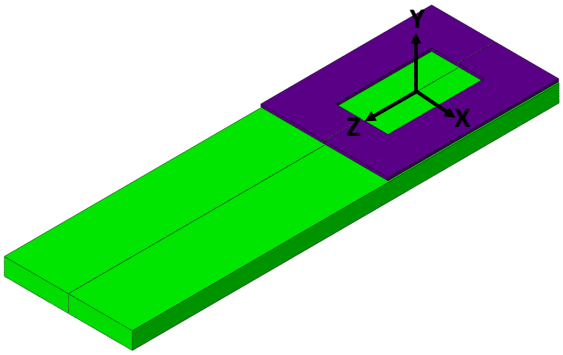

(a) SMA beam with rectangular coil geometry.

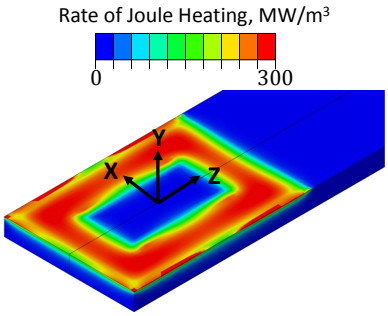

(b) Rate of Joule heating produced in the SMA by the rectangular coil.

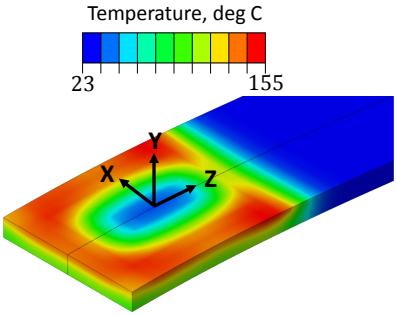

(c) Corresponding temperature profile in the SMA beam.

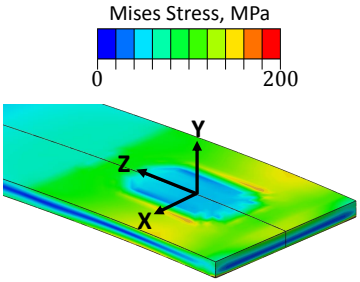

(d) Mises stress profile in the SMA beam due to a constant force of 75 N applied orthogonal to the beam axis and in the direction of the beam short dimension.

Figure 4.13: Homogenized 4 turn 20 AWG rectangular coil on an SMA beam. The beam is heated for 5 s using an RMS current of 40 A at 55 kHz

The Joule heating rate and maximum temperature at 5 s are significantly lower than in the beam with a circular coil, but the final displacement (referred to as the loaded cool condition) is the same, as shown in figure 4.14. Note that the circular coil produces lower temperature zones in the corners of the beam, which are absent for the rectangular coil. These lower temperature zones do not reach transformation and

cause only a portion of the beam to actuate. This leads to stress concentrations that are not seen with the rectangular coil. This result motivates future work focusing on detailed design optimization of the coupled actuator/coil configuration.

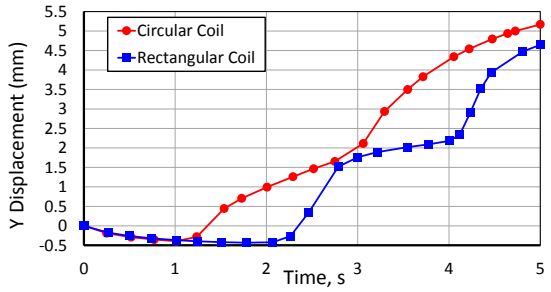

Figure 4.14: Vertical (Y-direction) tip displacement of the SMA beam with circular and rectangular coils. The beam is heated for 5 s using an RMS current of 40 A at 55 kHz. Displacement is referenced from as-loaded (cool) condition. A constant force of 75 N is applied orthogonal to the beam axis and in the direction of the beam short dimension.

4.3 Flux Concentrators

As described in section 1.4, magnetic flux concentrators offer numerous benefits that can improve the performance of an induction heating system. To this end, the effects of adding an MFC to the SMA based induction system are studied in a preliminary manner. Some authors note that even though MFCs are frequently used they are not well understood and can, in some cases, degrade performance of the induction system [70]. Note that work in in this section is purely numerical and completed only with the FE model. In this study any heating effects due to magnetic hysteresis and any temperature dependence in the permeability or resisitivity of the MFC are neglected. Initially, it may seem counter-intuitive that a high resistivity material would create a good flux concentrator but examining equations 2.45 and 2.46, it can

be noticed that the $\boldsymbol{J}_{e0}$ is proportional to $1/\rho$ as

$$\frac{1}{2}\rho|\boldsymbol{J}_{e0}|^2 = \frac{1}{2}\rho|\frac{j\omega}{\rho}\boldsymbol{A}_0|^2. \tag{4.2}$$

Before beginning any detailed design study, the FE model of an MFC must be verified. No experimental studies have been completed using MFCs so the FE model is compared to a publish solution [70]. In this paper a 10 cm long cylindrical workpiece with an outer diameter of 4 cm and inner diameter of 1 cm was modeled. This workpiece simulates the effects of work hardening where there is an inner magnetic core (thickness of 2.1 cm from the inner surface, relative permeability of 20) and an outer surface layer, which is assumed to be heated past the curie point (i.e. the relative permeability has decreased to 1). In this example there are two coils, both made of 1.5 x 2 x 0.24 cm rectangular copper tubing with 4.5 cm between the coil centers. One of the coil has an MFC around it made of a magneto-dielectric material (relative permeability of 60) that is 0.64 cm thick. The coil both have a current of 7000 A at 3 kHz. It is not specified whether this current is RMS or peak. In either case, the verification is intended to be qualitative rather than quantitative and a change in current will only alter the electromagnetic field magnitudes and not their distributions, which are of more importance here. The results of the verification are shown in figure 4.15.

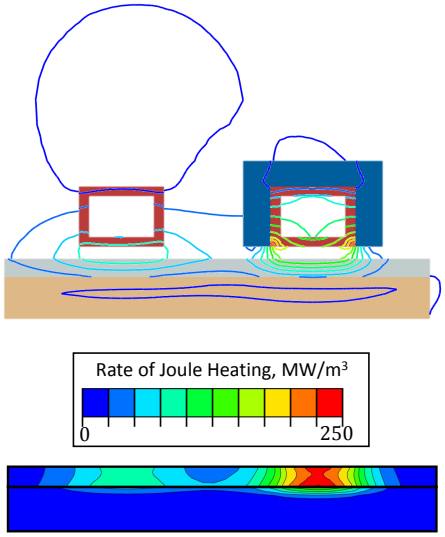

(a) Output from the FE model generated in this work based on the problem described. Upper portion of the figure shows the lines of constant magnetic field magnitude while the lower portion shows the heating power produced in the workpiece.

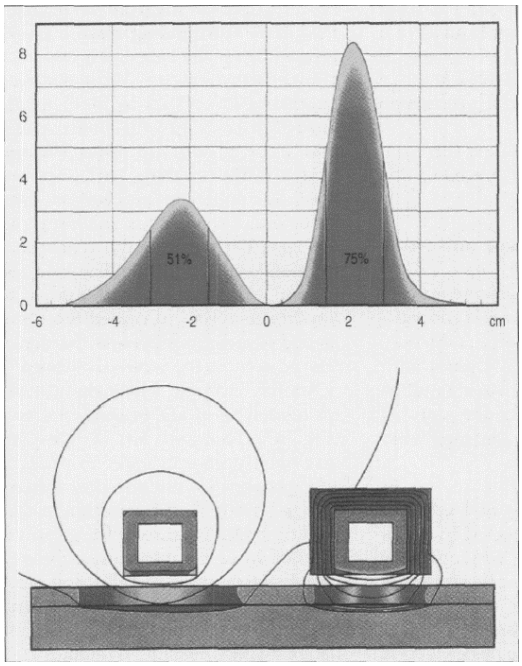

(b) Magnetic field magnitude contours with corresponding power distribution in the work piece is shown in the lower portion of the figure while the upper portion shows the surface power distribution [70].

Figure 4.15: Verification of FEA solution to a flux concentrator problem based on the work in [70].

It is not possible to exactly match the magnetic field magnitude contours because no data was given to do so but the behavior under the coils and in the workpiece closely matches between the FE model and published solution. As expected there is a prominent slot effect under the coil covered by the flux concentrator and in this region there is a more concentrated distribution of Joule heating power. When comparing the maximum surface values of the power given by the upper portion of

figure 4.15b to the values given in the lower portion of figure 4.15a, it can be seen that both indicate an increase in power of about 2.5 times when moving from the coil without an MFC to the coil with an MFC.

4.3.1 Design of Experiments

To determine approximate electromagnetic material properties that are desired in a flux concentrator, a design of experiments (DoE) study is used on the same tube described in section 3 (8 in. (203 mm) length with outer and inner diameters of 0.375 in. (9.525 mm) and 0.225 in. (5.715 mm)). The tube has a 14 AWG copper wire coil tightly wound around it with an RMS current of 35 A at 50 kHz. The flux concentrator is placed at two locations, internal to the tube and external. In both cases the flux concentrator thickness is be varied and but its length is fixed equal to the SMA tube length. The relative permeability and resistivity are also be varied. The design points used are listed in table 4.1. Recall that the SMA tube has a relative permeability of approximately 1 and resistivity of approximately 10^{-6} respectively. The thickness of the internal MFC was limited by the inner diameter of the tube.

Table 4.1: Design points used in DoE study.

Thickness (mm)	**Resistivity (Ω-m)**	**Relative Permeability**
	(External Concentrator)	
0.5	10^{-8}	1
1	10^{-6}	10
2.5	10^{-3}	100
4	1	1000
	100	
	(Internal Concentrator)	
0.5	10^{-8}	1
1	10^{-6}	10
1.5	10^{-3}	100
	1	1000
	100	

The results of the DoE are shown in figure 4.16. Each combination of points for the internal and external concentrators are shown plotted against the normalized rate of Joule heating, which is the average rate of Joule heating of each point through the thickness with an MFC compared to the average rate of Joule heating through the thickness of a case without an MFC.

To determine the effect of each variable, the main effects are computed by taking the mean of the normalized average Joule heating for all results using a particular variable at a particular value then subtracting the mean of the normalized average Joule heating for all results (i.e. all results using a thickness of 1.0 mm are averaged and the total average is subtracted from this). The main effects are shown graphically in figure 4.17.

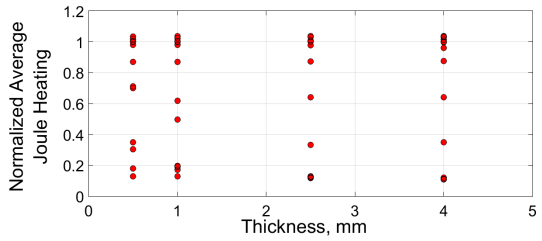

(a) Result of a changing thickness on normalized rate of Joule heating using an external MFC.

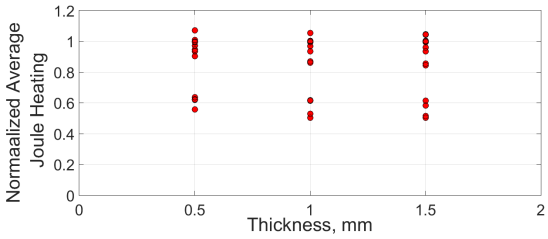

(b) Result of a changing thickness on normalized rate of Joule heating using an internal MFC.

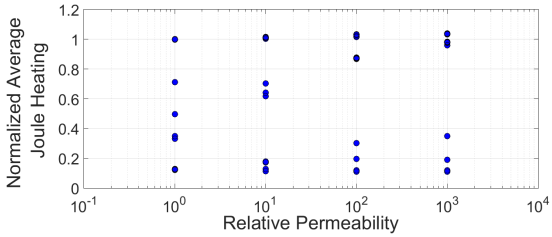

(c) Result of a changing relative permeability on normalized rate of Joule heating using an external MFC.

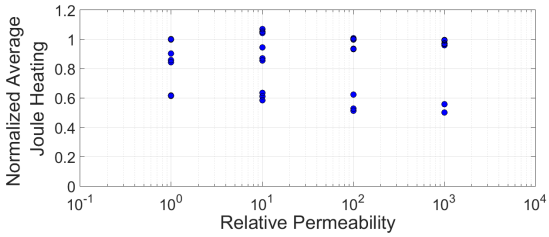

(d) Result of a changing relative permeability on normalized rate of Joule heating using an internal MFC.

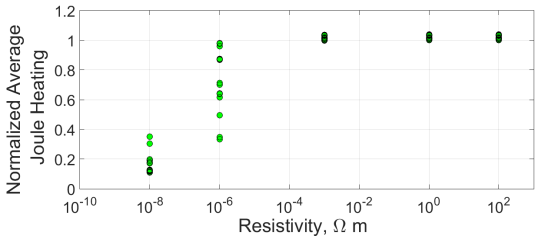

(e) Result of a changing resistivity on normalized rate of Joule heating using an external MFC.

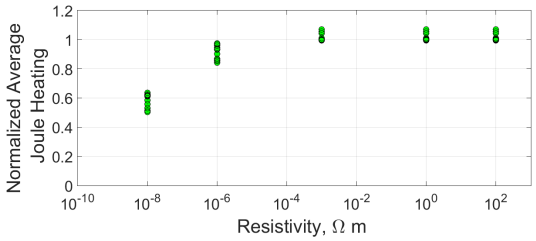

(f) Result of a changing resistivity on normalized rate of Joule heating using an internal MFC.

Figure 4.16: Results of the DoE study for the internal and external MFC. Each point corresponds to one design combination.

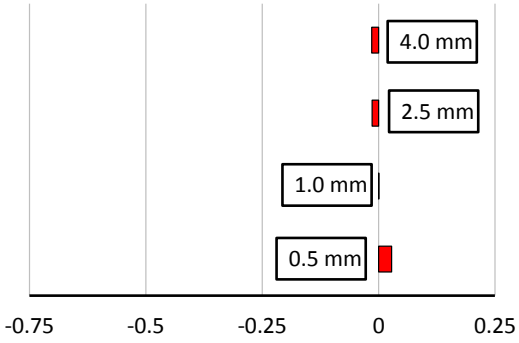

(a) Effect of thickness on normalized rate of Joule heating using an external MFC.

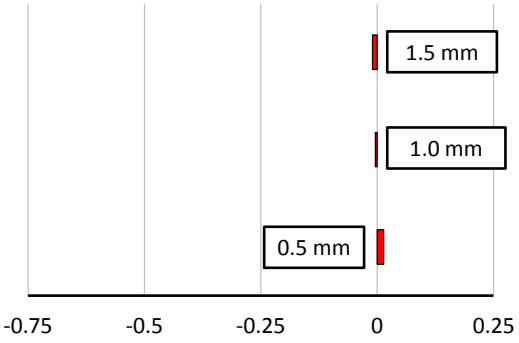

(b) Effect of thickness on normalized rate of Joule heating using an internal MFC.

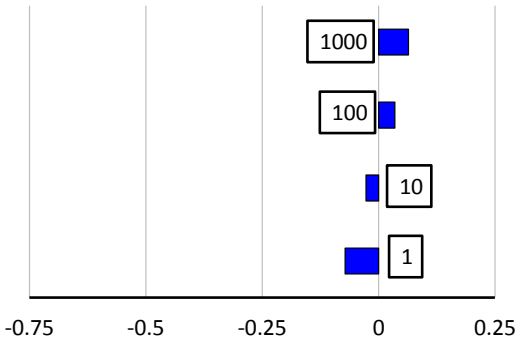

(c) Effect of relative permeability on normalized rate of Joule heating using an external MFC.

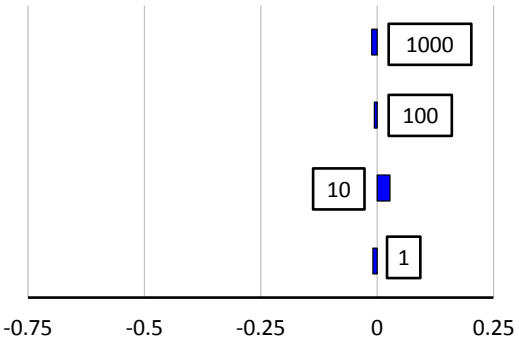

(d) Effect of relative permeability on normalized rate of Joule heating using an internal MFC.

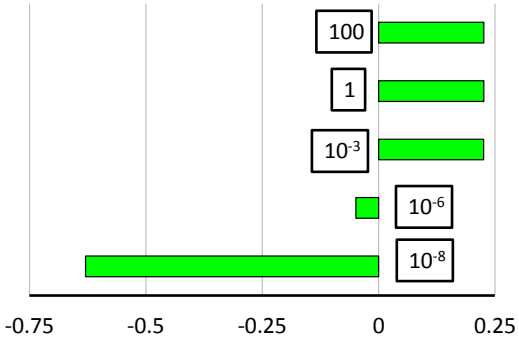

(e) Effect of resistivity on normalized rate of Joule heating using an external MFC.

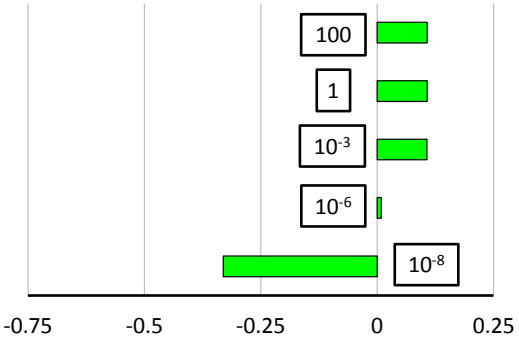

(f) Effect of resistivity on normalized rate of Joule heating using an internal MFC.

Figure 4.17: Main effects plots of the DoE study for the internal and external MFC.

The results of the DoE indicate that there is not a significant effect of thickness on the internal or external MFC. Both showed that a thinner concentrator has a slightly higher effect on the normalized average Joule heating. The relative permeability, like the thickness, has a small effect on the results for both the internal and external MFC cases. An unusual result that is seen in the effect of the permeability on an internal MFC is that only a relative permeability of 10 has a positive effect when it is expected that as permeability increases the effect should increase positively as is seen by the external MFC permeability effect. This could indicate that some interaction effects are occurring that are not being considered. Unlike the thickness and permeability, the resistivity has a clear effect that shows after the MFC resistivity is increased beyond that of the SMA the normalized average Joule heating always has a relatively large positive effect as expected.

Looking beyond just the normalized rate of Joule heating, the heating field through the thickness can be visualized as shown in figure 4.18 to determine how a flux concentrator will effect the radial gradients involved in induction heating. From this figure, it can be seen that an external concentrator can only have the effect of increasing or decreasing the magnitude of the Joule heating power. When the internal concentrator is examined, it is seen to have a dramatic effect on the distribution of Joule heating through the thickness and effectively make the distribution of heating through the thickness uniform. The implication of this effect is that is a system can be realized, which realizes the high heating rate of induction heating while reducing the thermal gradients through the thickness of the tube. Furthermore this MFC induced behavior could be coupled with the frequency induced behavior shown in figure 4.9 to create heating scenarios and distributions not previously possible.

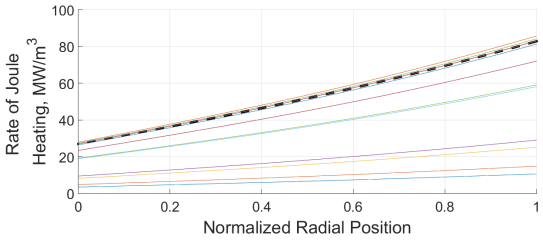

(a) Distribution of Joule heating power through the thickness of the tube using an external MFC for each set of points in the DoE.

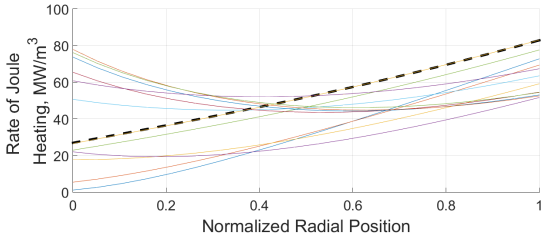

(b) Distribution of Joule heating power through the thickness of the tube using an internal MFC for each set of points in the DoE.

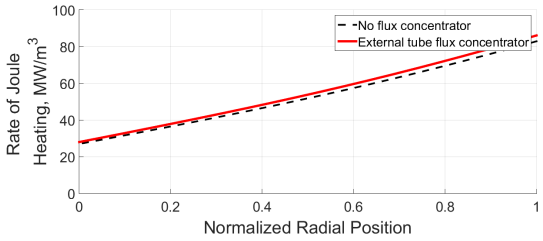

(c) Highest normalized Joule heating external MFC case from the DoE.

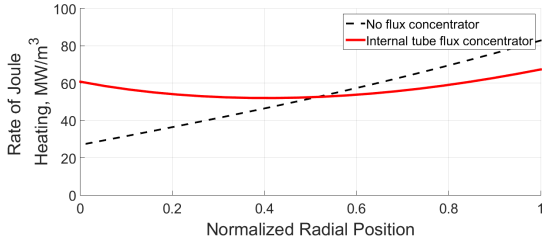

(d) Highest normalized Joule heating internal MFC case from the DoE.

Figure 4.18: Joule heating distribution through the tube thickness compared to the baseline no MFC case (shown as a thick dashed line).

The best case scenarios of figures 4.18c and 4.18d represent the case in the DoE where the resistivity and permeability were highest and the thickness was the lowest. The best cases for the internal and external MFCs can be used to run a complete electromagnetic-thermo-mechanical analysis in the FE model developed to get the result shown in figure 4.19. From this figure, it can be seen that the internal concentrator, which greatly redistributes the Joule heating also produces the highest temperature after 5 s of heating. Using an external MFC also produces an increase in temperature after 5 s of heating relative to the case not using an MFC. The increases in final temperatures are about 3% higher using an external MFC and about

7% higher using an internal concentrator. As these MFCs are typically made of iron based ferrites, they add a significant amount of mass to the system, which in aerospace based systems may not be worth the small reduction in heating time need to reach a goal temperature.

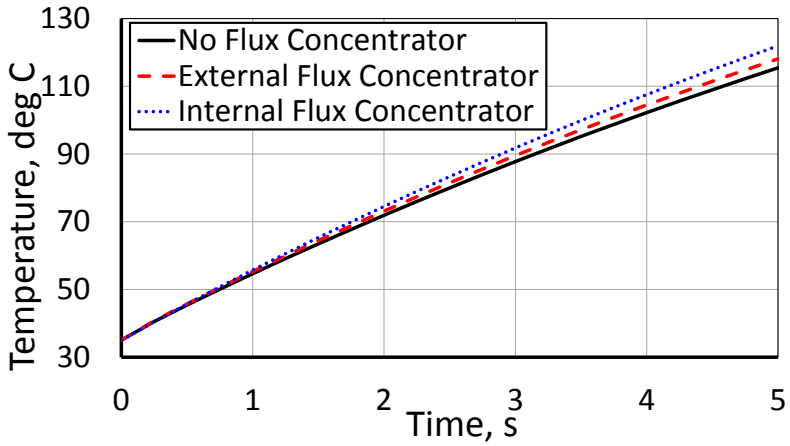

Figure 4.19: Outer surface temperature at the mid-length of the SMA tube over 5 s subject to heating from a 14 AWG tightly wound solenoid with an RMS current of 35 A at 50 kHz. The best case internal and external MFCs are compared to a case without an MFC. A small improvement in heating can be noticed.

4.3.2 Torque Tube Study

Now that the properties and effects of an MFC have been examined, those results can be used to further study how the position and size of the MFC effects the results. The tube has not changed from the DoE study and still has a 14 AWG tightly wound copper wire coil around it with an RMS current of 35 A at 50 kHz. The flux concentrator is taken to have a resistivity of $10^8\,\Omega$-m and a relative permeability

of 1000 with a thickness of 0.5 mm. The flux concentrator is placed at 6 positions relative to the SMA and coil shown in figure 4.20.

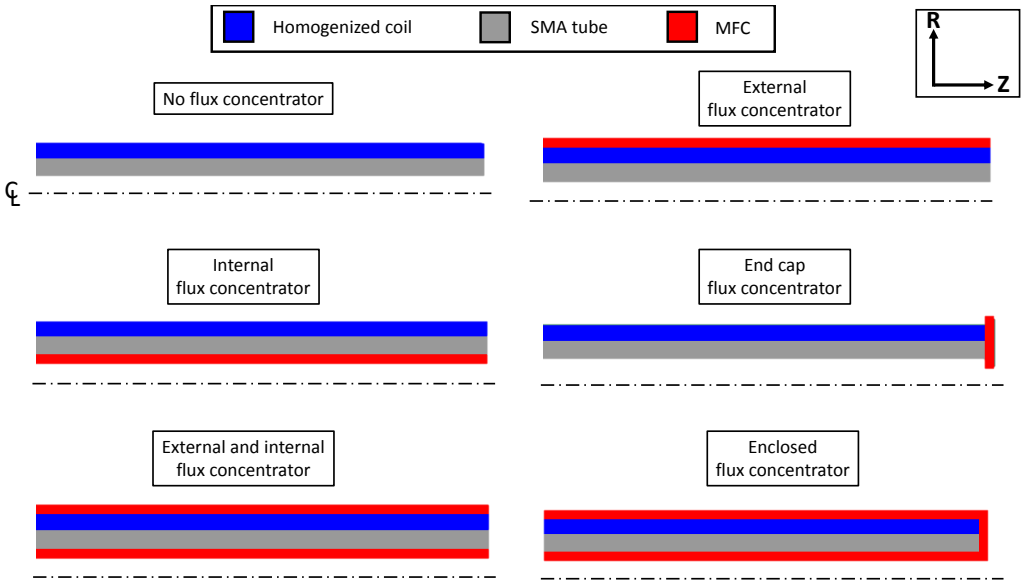

Figure 4.20: MFC positions relative to the SMA tube and coil. Only the end portion of the tube is shown.

The magnetic and electric fields generated by this setup are shown in figure 4.21. Examining the generated electric fields, the same behavior that was shown in figure 4.4a is seen where there is a large free electric field around the coil. The addition of a flux concentrator external to the coil allows the field to be blocked, which could be beneficial if an induction system is used in conjunction with any electronic sensing equipment. When the case of an internal concentrator is examined it can be seen that, as before, the fields are concentrated on the inner surface of the SMA tube rather than the outer surface and there is a more uniform distribution created. A particularly interesting case is the enclosed flux concentrator where the fields in the SMA become completely uniform along the length of the tube giving the solution that would be expected for an infinitely long tube where there are no end effects. Note that in the case of both an external and internal MFC, there is a reduction in the end effect at the end of the SMA tube.

The rate of Joule heating generated in the SMA by the fields of figure 4.21 is shown in figure 4.22. The same effects as before can be noticed in the heating patterns. An external MFC tends to increase the magnitude of the heating through the thickness while an internal MFC redistributes the fields through the thickness. A combination of the internal and external MFCs shows a combination of these effects and an end cap tends to reduce the edge effects only at the end of the tube.

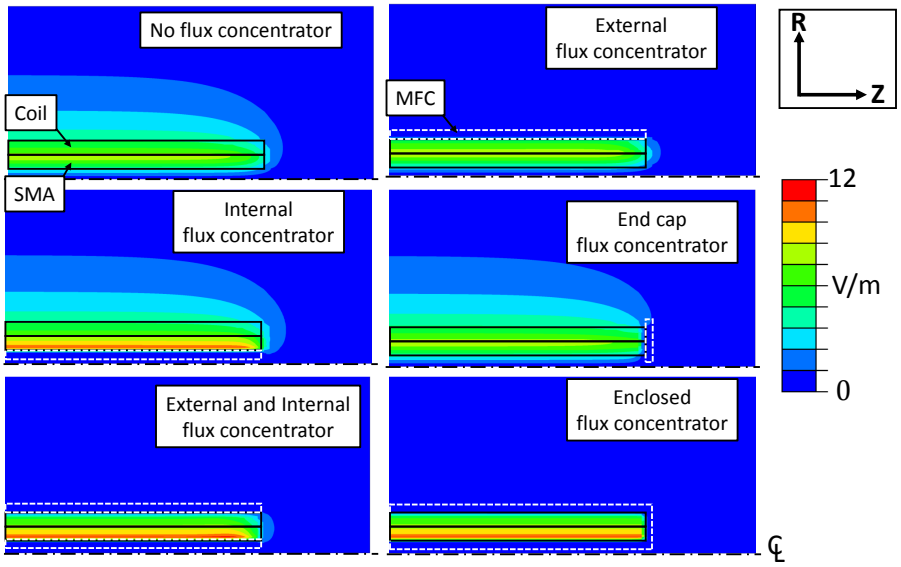

(a) Electric field magnitude generated in the SMA tube.

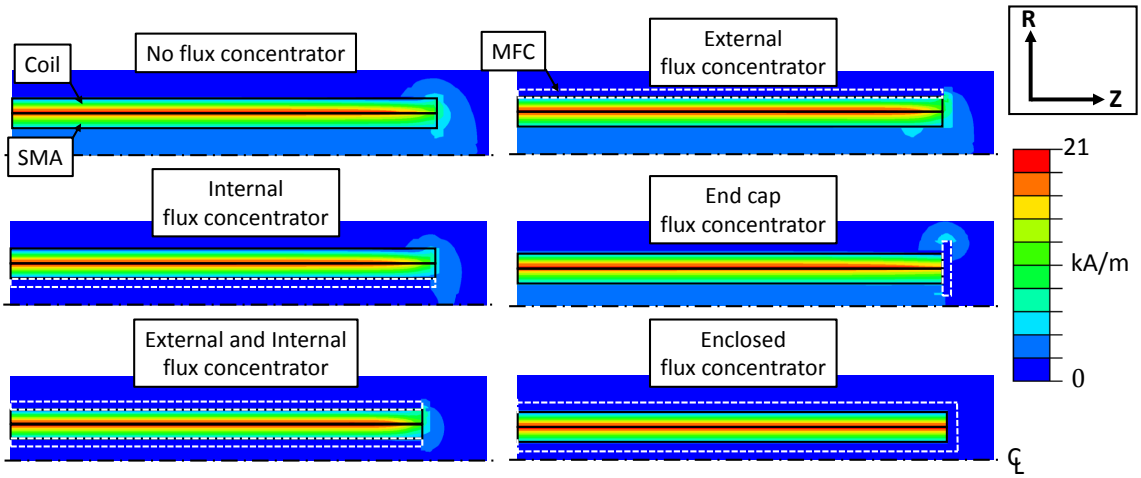

(b) Magnetic field magnitude generated in the SMA tube.

Figure 4.21: Electromagnetic fields generated by an RMS current of 35 A at 50 kHz in a 14 AWG solenoid. MFC positions relative to the SMA tube are identified with a dashed white line.

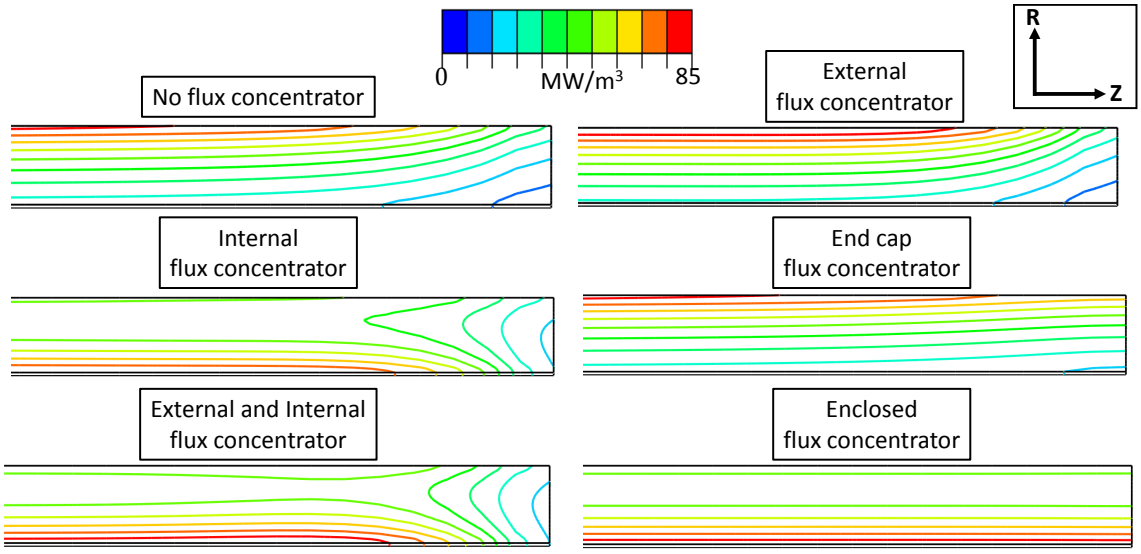

Figure 4.22: Rate of Joule heating contours in the SMA tube with varying MFC positions.

If this rate of heating is integrated over the SMA body, an effective power in the SMA tube and be found. This integration is summarized in table 4.2. As expected the enclosed flux concentrator shows the highest power and the internal/external MFC combination shows the next highest power level. An unexpected result is that the power in the internal MFC case is actually lower than the power in the external MFC case, which counter-intuitive after examining figure 4.19 where the internal concentrator showed a higher temperature after heating. The unexpected behavior is likely being caused by the same behavior that resulted in a high permeability having a negative effect on the internal MFC. The internal concentrator with the ability redistribute the Joule heating fields has an unusual predicted behavior that requires further examination to fully understand.

Table 4.2: Real power in the SMA tube after integrating the rate of Joule heating over the body.

	SMA Power (W)	**Difference**[†] (%)
No MFC	464	-
External MFC	484	4.32
Internal MFC	479	3.06
External and Internal MFC	495	6.56
End Cap MFC	469	0.97
Enclosed MFC	500	7.58

[†] Relative to the power in the SMA without an MFC.

4.3.3 Plate Study

To further examine the effects of an MFC in a problem where the fields are not concentrated well, as is the case with a tube and solenoid setup, a square SMA plate is studied with a width and length of 7 in. (12.7 cm). The plate thickness is varied between a thick plate (0.25 in. (6.35 mm)) and a thin plate (0.1 in. (2.54 mm)) to the determine how the effect of SMA thickness effects the electromagnetic fields. The induction coil in this study has an outer diameter of 2 in. (5.08 cm), and inner diameter of 0.5 in. (1.27 cm), and a thickness of 0.1 in. (2.54 mm) with an applied RMS current of 35 A. The frequency is varied between 50 kHz in the thick plate and 5 kHz in the thin plate. A solid disk flux concentrator is applied with the same outer diameter as the coil and has the same properties as the previous tube study. The MFC is placed either directly on top of the coil, in line with the coil on the opposite side of the SMA, or a combination of both as shown in figure 4.23. Note that MFCs placed adjacent to the coil directly on top of the SMA were also studied but the results showed that there was not effect, even when placing the MFC directly next to the coil thus the results are omitted.

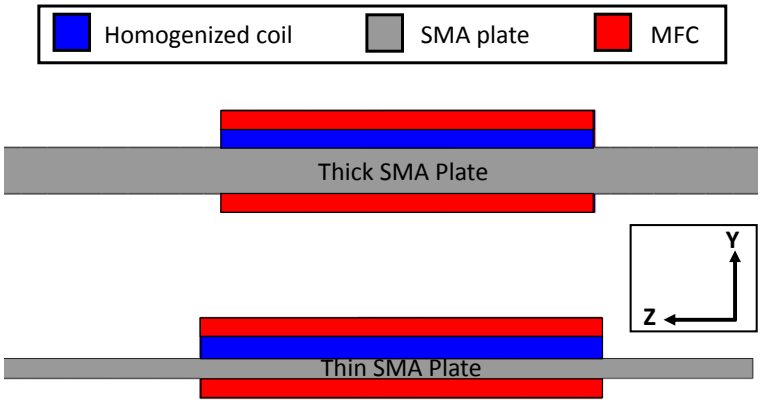

Figure 4.23: SMA plate study geometry. The coil is placed on top of the SMA and a disk flux concentrator is placed either above the coil, below the SMA in line with the coil, or a combination of both. An enhanced side view of the plate is shown with the coil and MFC but the plate studied extends far beyond what is shown to elminate end effects.

The magnetic field and corresponding heating profile in the SMA for the thick plate is shown in figure 4.24 with the thin plate shown in figure 4.25. In the thick plate case, a large free magnetic field around the coil can be noticed, which is not contributing to heating the SMA body. It can also be seen that the fields do not penetrate through the plate so that a bottom flux concentrator has no effect. As the bottom MFC has no effect the case using both a bottom and top MFC is the same as using only the concentrator on top of the coil. The top concentrator shows promise as a means to improve performance of the induction system by greatly improving the rate of heating in the SMA Body.

If the thin plate case is examined where the frequency is lower and thus skin depth (equation 1.1) is higher, there is a much less concentrated magnetic field around

the SMA body. Specifically, it can be seen that a portion of the magnetic field has penetrated through the plate thus the bottom MFC now helps to concentrate this field in the SMA plate. Comparing the case of the top concentrator and combined concentrator, a similar pattern is seen indicating that the MFC above the coil still dominates the system. When the heating profile through the thickness is examined, it can be seen that a bottom concentrator has the effect of "pulling" the heat flux through the plate while the top concentrator has the effect of "pushing" the heat flux through, as was seen in the SMA tube, and when the effects are combine a heating rate that is up to ten times greater than the case not using an MFC can be achieved. This demonstrates that it is possible to generate heating using a low frequency, thus low power, that is comparable in magnitude to the rate of heating that would be achieved by use of a much higher frequency.

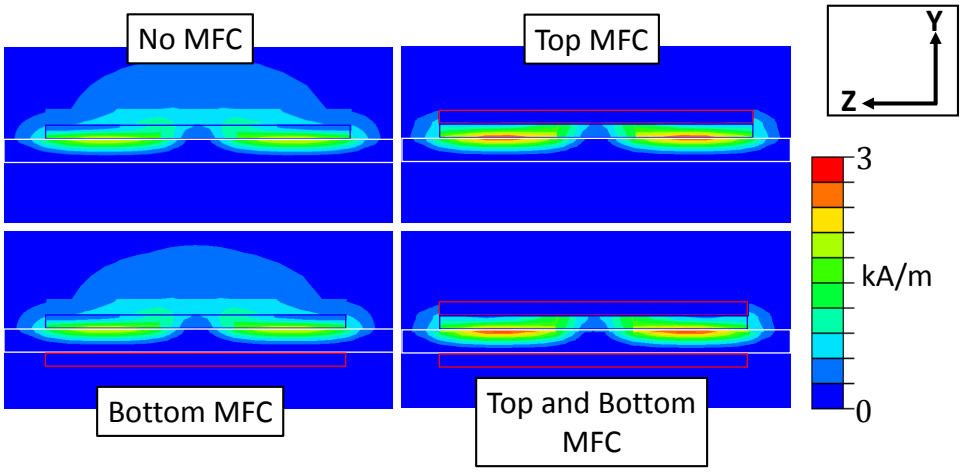

(a) Magnetic field magnitude around the thick SMA plate.

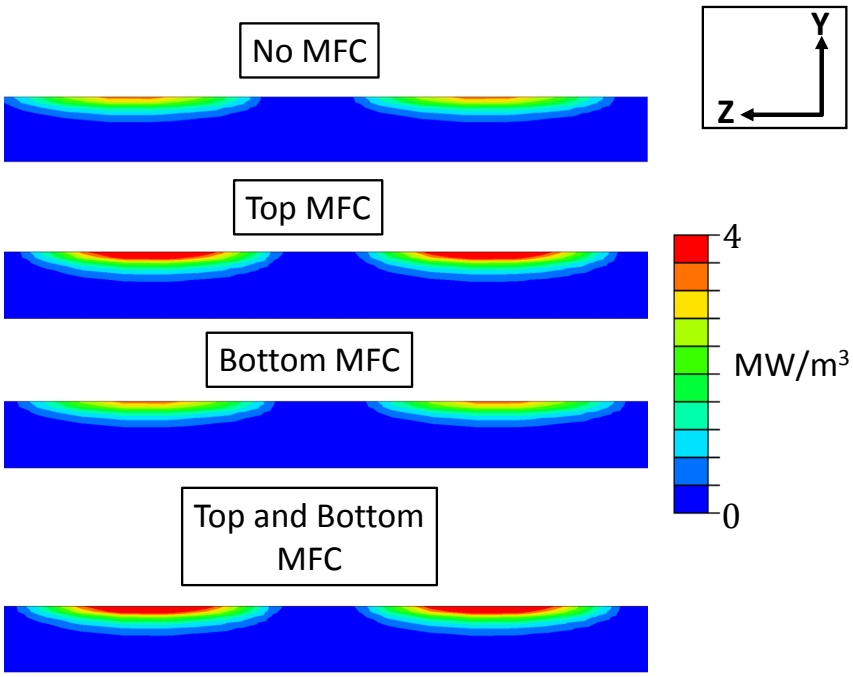

(b) Rate of Joule heating profile produced in the thick SMA plate.

Figure 4.24: Thick SMA plate study results generated by applying an RMS current of 35 A at 50 kHz to the coil.

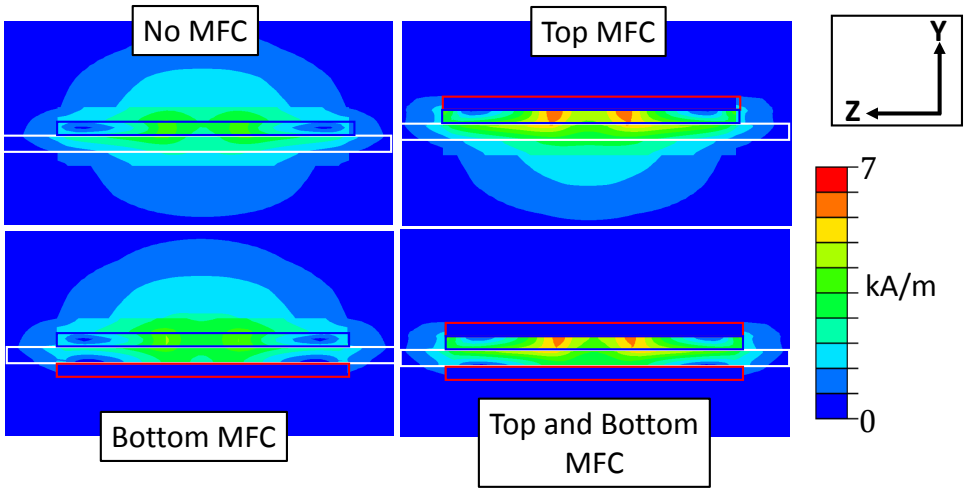

(a) Magnetic field magnitude around the thin SMA plate.

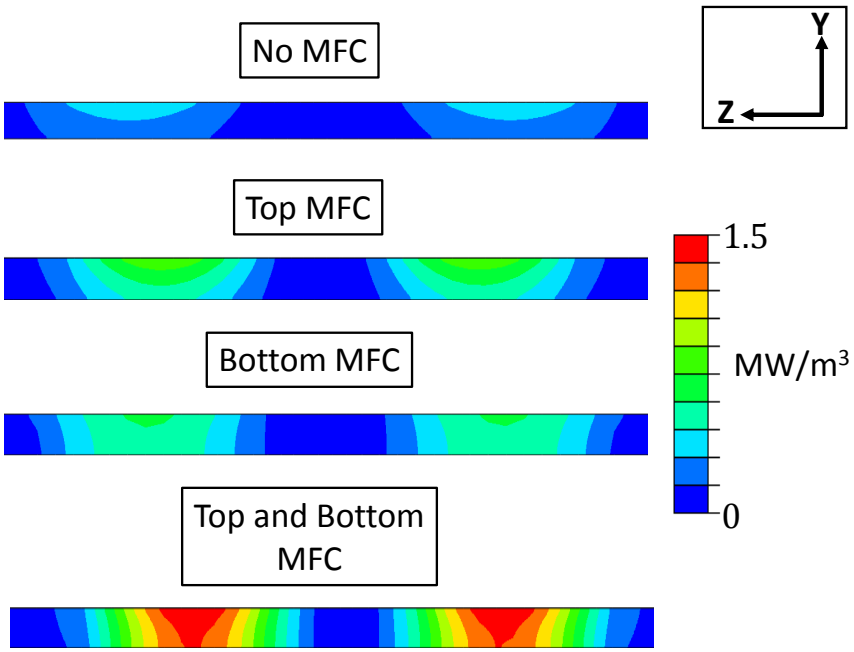

(b) Rate of Joule heating profile produced in the thin SMA plate.

Figure 4.25: Thin SMA plate study results generated by applying an RMS current of 35 A at 5 kHz to the coil.

A quantity of interest that should be studied more in the future is the ratio of skin depth to SMA wall thickness. For the thick plate this value is 0.32 while in the thin plate it is 2.5. This ratio could determine whether an MFC on the bottom of the SMA would be beneficial. If this ratio is grater than 1, it would indicate a substantial amount of the magnetic field is penetrating through the body and an MFC could recapture a portion of the permeating field to achieve an increased heating rate.

4.3.4 Application to an SMA Bending Beam

To study the effects of an MFC in an actual system, the SMA beam model of section 4.2 using a circular coil is recalled. A 0.5 mm thick solid disk concentrator made of NiZn ferrite [56, 79, 58] is placed above the 12 turn 20 AWG copper wire coil in the same manner as before. The coil again has an RMS coil current of 40 A at 55 kHz. Here only a top concentrator is studied as the skin depth (3.8 mm) was not greater than the beam thickness (5.1 mm) therefore a bottom concentrator would likely have no effect. A NiZn ferrite can have large variations in material properties; for this work a relative magnetic permeability of 1500 and a resistivity of 10^7 Ω-cm [58] is chosen, which makes an excellent MFC based on the results of the previous DoE. No inputs to the system or dimensions were changed from the analysis that generated figure 4.12. The results shown in figure 4.26 indicate a dramatic increase in heating rate relative to the case without a flux concentrator as expected based on the prior plate study.

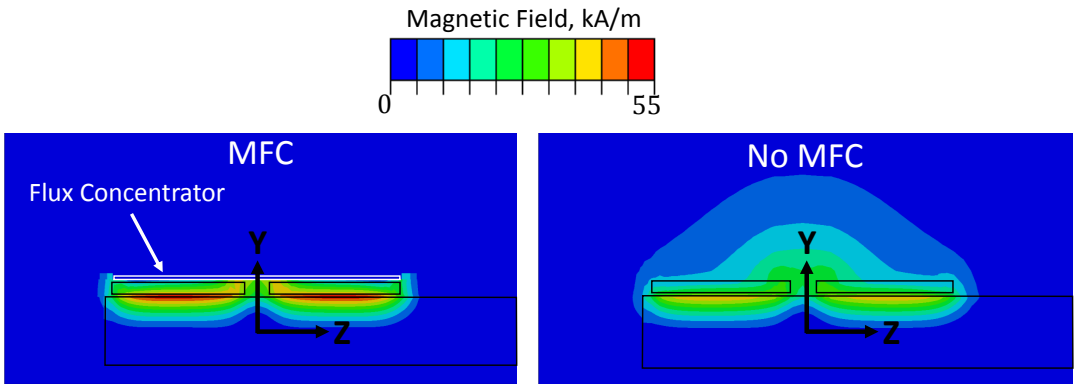

(a) Magnetic field magnitude

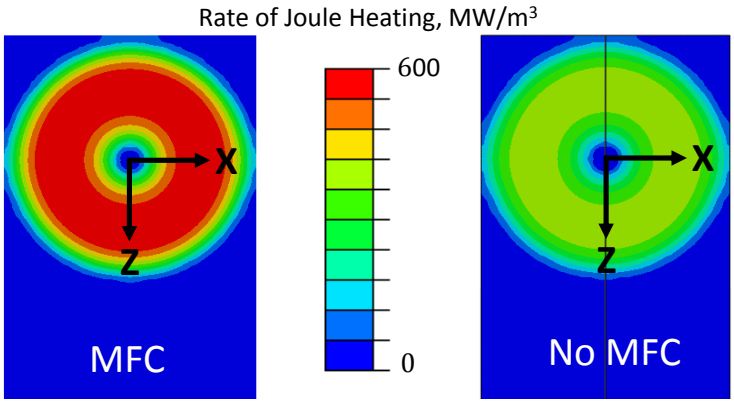

(b) Rate of Joule heating

Figure 4.26: Electromagnetic fields with and without a NiZn flux concentrator above the coil. The coil is a homogenized 12 turn 20 AWG circular coil with an applied RMS current of 40 A at 55 kHz.

5. CONCLUSIONS

This thesis has shown the development of a model that can analyze the coupled electormagnetic-thermo-mechanical behavior of an arbitrarily shaped monolithic SMA component undergoing induction heating. The model developed was implemented in Abaqus Unifed FEA for analysis of general 3-D SMA bodies and reduced to an ordinary differential equation in time for the case of a thin walled SMA tube heating by a long solenoid. Section 2 showed a complete derivation of both the FE model and ODE solution including how each model was implemented. Following this section 3 showed a calibration of both models to a specific experimental SMA tube used throughout the work. The results showed that the ODE solution agreed well with the calibrated FE model without manipulation and the FE model agreed well with experiments. In section 4 both the FE model and ODE solution were tested against two experimental setups. The first test showed that the FE model was able to capture a varying experimental input power in the induction system well. The ODE solution was able to capture some of the behavior but generally overestimated the rate of heating. In the second test, a high rate actuation study was conducted where a tube was heated with induction and cooled using an active liquid flow. After some calibration for cooling both models were able to capture the behavior noticed in this study well. Following the experimental validation of the models, the FE model was used to examine the effects of a changing frequency to show how radial gradients in the SMA could be controlled by the induction system frequency. These effects can be used to improve actuator performance and training. Following the SMA tube study, an SMA beam study was conducted again using the FE model. This study showed how a changing coil shape can effect the heating of the SMA actuator being used by

creating a different temperature profile distribution. In the final section of section 4, a thorough analysis of flux concentrators was conducted. This analysis included a design of experiments to determine the appropriate properties that an MFC would possess. The analysis also included a study of an SMA tube and plate to determine how workpiece shape, relative coil position, and MFC postion and shape could effect the system. The MFC study results were then applied to the SMA beam study and showed a drastic improvement in the rate of heating achieved in the SMA beam.

Future work should focus on using the models developed to improve actuation systems incorporating inductively heated SMA tubes and beams by considering the SMA actuator, induction system, flux concentrators, cooling system, and electrical power source. To do this, the FE model should be coupled in the same manner as the ODE solution where feedback from the thermo-mechanical problem is considered in the electromagnetic problem. Additionally, latent heat should be considered in the FE thermo-mechanical model to better capture the behavior in time of the SMA component. The addition of the thermal-electric effects of resistive heating in the induction coil should be studied so that conduction to/from the SMA due to the coil can be simulated. Further work should include increasing the ODE solution to a 1-D model where only radial effects in the SMA tube are considered. A 1-D model such as this should be able to much more accurately describe the behavior of an SMA tube being inductively heated while reducing computational time. Reduced order models should also be completed for the cases of an SMA tube using an MFC and an SMA beam or plate. Closed form solutions exist for planar coil induction heating and for systems which have components of varying magnetic properties. It is important in induction heating to consider all aspects of the heating and actuation system as well as interactions between them. Before implementing any induction system using SMA actuators, detailed studies should be conducted to prevent any

unexpected results due to the interaction between the electromagnetic fields and the system components. Until the development of this model such detailed analyses were not possible and thus performance of the actuation system was not being maximized.

REFERENCES

[1] Abaqus. *Abaqus 6.13 Online Documentation*. Dassault Systemes of America Corp., 2013.

[2] F Bay, V Labbé, Y Favennec, and JL Chenot. A numerical model for induction heating processes coupling electromagnetism and thermomechanics. *International journal for numerical methods in engineering*, 58(6):839–867, 2003.

[3] BC Bayer, S Sanjabi, C Baehtz, CT Wirth, S Esconjauregui, RS Weatherup, ZH Barber, S Hofmann, and J Robertson. Carbon nanotube forest growth on niti shape memory alloy thin films for thermal actuation. *Thin Solid Films*, 519(18):6126–6129, 2011.

[4] CL Bertagne, DJ Hartl, and TJ Cognata. Analysis of highly coupled thermal-structural responses in morphing radiative bodies.

[5] CL Bertagne, RB Sheth, DJ Hartl, and JD Whitcomb. Simulating coupled thermal-mechanical interactions in morphing radiators. In *SPIE Smart Structures and Materials+ Nondestructive Evaluation and Health Monitoring*, pages 94312F–94312F. International Society for Optics and Photonics, 2015.

[6] NT Birch and JR Webster. Gas turbine engine exhaust nozzle having a noise attenuation device driven by shape memory material actuators, November 9 2004. US Patent 6,813,877.

[7] AF Bower. *Applied Mechanics of Solids*. CRC press, 2011.

[8] JG Boyd and DC Lagoudas. A thermodynamical constitutive model for shape memory materials. Part I. the monolithic shape memory alloy. *International Journal of Plasticity*, 12(6):805–842, 1996.

[9] LC Brinson, A Bekker, and S Hwang. Deformation of shape memory alloys due to thermo-induced transformation. *Journal of Intelligent Material Systems and Structures*, 7(1):97–107, 1996.

[10] PR Buckley, GH McKinley, TS Wilson, W Small, WJ Benett, JP Bearinger, MW McElfresh, and DJ Maitland. Inductively heated shape memory polymer for the magnetic actuation of medical devices. *Biomedical Engineering, IEEE Transactions on*, 53(10):2075–2083, 2006.

[11] WJ Buehler and FE Wang. A summary of recent research on the nitinol alloys and their potential application in ocean engineering. *Ocean Engineering*, 1(1):105–120, 1968.

[12] J Butler, P Tiernan, AA Gandhi, S Beloshapkin, and SAM Tofail. Processing of small scale nitinol billets by induction heated nonconventional isothermal extrusion (ihncie). *Journal of Engineering Materials and Technology*, 133(2):021009, 2011.

[13] B Carpenter and J Lyons. Eo-1 technology validation report: Lightweight flexible solar array experiment. *NASA/GSFC. Last updated: August*, 8, 2001.

[14] JC Chen and B Wiscombe. Use of shape memory alloy for internally fixing light emitting device at treatment site, June 27 2000. US Patent 6,080,160.

[15] TJ Cognata, DJ Hartl, R Sheth, and C Dinsmore. A morphing radiator for high-turndown thermal control of crewed space exploration vehicles. 2014.

[16] BD Coleman and W Noll. The thermodynamics of elastic materials with heat conduction and viscosity. *Archive for Rational Mechanics and Analysis*, 13(1):167–178, 1963.

[17] BD Coleman and W Noll. Material symmetry and thermostatic inequalities in finite elastic deformations. *Archive for Rational Mechanics and Analysis*, 15(2):87–111, 1964.

[18] M Collet, E Foltête, and C Lexcellent. Analysis of the behavior of a shape memory alloy beam under dynamical loading. *European Journal of Mechanics-A/Solids*, 20(4):615–630, 2001.

[19] D Cui, G Song, and H Li. Modeling of the electrical resistance of shape memory alloy wires. *Smart Materials and Structures*, 19(5):055019, 2010.

[20] J Davies and P Simpson. *Induction Heating Handbook*. McGraw-Hill London, 1979.

[21] AC Eringen. Continuum theory of micromorphic electromagnetic thermoelastic solids. *International Journal of Engineering Science*, 41(7):653–665, 2003.

[22] JD Ertel and SA Mascaro. Dynamic thermomechanical modeling of a wet shape memory alloy actuator. *Journal of Dynamic Systems, Measurement, and Control*, 132(5):051006, 2010.

[23] M Fisk. *Simulation of Induction Heating in Manufacturing*. PhD thesis, Division of Material Mechanics, Luleå University of Technology, 2008.

[24] J Frenzel, Z Zhang, K Neuking, and G Eggeler. High quality vacuum induction melting of small quantities of niti shape memory alloys in graphite crucibles. *Journal of Alloys and Compounds*, 385(1):214–223, 2004.

[25] EA Giroux, M Maglione, A Gueldry, and JL Mantoux. Electromagnetic heating of a shape memory alloy translator. *Journal of Physics D: Applied Physics*, 29(3):923, 1996.

[26] RF Hamilton, H Sehitoglu, Y Chumlyakov, and HJ Maier. Stress dependence of the hysteresis in single crystal niti alloys. *Acta Materialia*, 52(11):3383–3402, 2004.

[27] DJ Hartl, B Kiefer, and A Menzel. Modeling shape memory alloy single crystalline responses using an anisotropic yield surface. *TMS2013 Supplemental Proceedings*, pages 975–986, 2013.

[28] DJ Hartl and DC Lagoudas. Aerospace applications of shape memory alloys. *Proceedings of the Institution of Mechanical Engineers, Part G: Journal of Aerospace Engineering*, 221(4):535–552, 2007.

[29] DJ Hartl and DC Lagoudas. Constitutive modeling and structural analysis considering simultaneous phase transformation and plastic yield in shape memory alloys. *Smart Materials and Structures*, 18(10):104017, 2009.

[30] DJ Hartl, DC Lagoudas, and FT Calkins. Advanced methods for the analysis, design, and optimization of SMA-based aerostructures. *Smart Materials and Structures*, 20(9):094006, 2011.

[31] DJ Hartl, DC Lagoudas, FT Calkins, and JH Mabe. Use of a ni60ti shape memory alloy for active jet engine chevron application: I. thermomechanical characterization. *Smart Materials and Structures*, 19(1):015020, 2010.

[32] DJ Hartl, JT Mooney, DC Lagoudas, FT Calkins, and JH Mabe. Use of a ni60ti shape memory alloy for active jet engine chevron application: Ii. experimentally validated numerical analysis. *Smart Materials and Structures*, 19(1):015021, 2010.

[33] DJ Hartl, A Solomou, DC Lagoudas, and D Saravanos. Phenomenological modeling of induced transformation anisotropy in shape memory alloy actuators. In

SPIE Smart Structures and Materials+ Nondestructive Evaluation and Health Monitoring, pages 83421M–83421M. International Society for Optics and Photonics, 2012.

[34] M Hediehloo and M Akhbari. New approach in design of planar coil of induction cooker based on skin and proximity effects analysis. In *Industrial Technology, 2009. ICIT 2009. IEEE International Conference on*, pages 1–6. IEEE, 2009.

[35] J Herrington, L Hodge, C Stein, Y Babbar, RN Saunders, DJ Hartl, and JH Mabe. Development of a twisting wing powered by a shape memory alloy actuator. In *AIAA SciTech*. American Institute of Aeronautics and Astronautics Inc., 2015.

[36] JP Holman. *Heat Transfer*. Mc Graw–Hill Book Company, 1986.

[37] S Huang, M Leary, T Ataalla, K Probst, and A Subic. Optimisation of ni–ti shape memory alloy response time by transient heat transfer analysis. *Materials & Design*, 35:655–663, 2012.

[38] PV Hull, SL Canfield, and C Carrington. A radiant energy-powered shape memory alloy actuator. *Mechatronics*, 14(7):757–775, 2004.

[39] WS Janna. *Engineering Heat Transfer*. CRC Press, 1999.

[40] Hyoung Y Jun, Othon K Rediniotis, and Dimitris C Lagoudas. Development of a fuel-powered shape semory alloy actuator system: I. numerical analysis. *Smart Materials and Structures*, 16(1):S81, 2007.

[41] Hyoung Y Jun, Othon K Rediniotis, and Dimitris C Lagoudas. Development of a fuel-powered shape semory alloy actuator system: Ii. fabrication and testing. *Smart Materials and Structures*, 16(1):S95, 2007.

[42] Y Kabiri, A Kermanpur, and A Foroozmehr. Comparative study on microstructure and homogeneity of niti shape memory alloy produced by copper boat induction melting and conventional vacuum arc melting. *Vacuum*, 86(8):1073–1077, 2012.

[43] AC Keefe and GP Carman. Thermo-mechanical characterization of shape memory alloy torque tube actuators. *Smart Materials and Structures*, 9(5):665, 2000.

[44] DK Kennedy, FK Straub, L McD Schetky, Z Chaudhry, and R Roznoy. Development of an SMA actuator for in-flight rotor blade tracking. *Journal of Intelligent Material Systems and Structures*, 15(4):235–248, 2004.

[45] D Lagoudas, Z Bo, M Qidwai, and P Entchev. SMA um: User material subroutine for thermomechanical constitutive model of shape memory alloys. *Texas A&M University College Station TX*, 2003.

[46] DC Lagoudas. *Shape Memory Alloys: Modeling and Engineering Applications*. Springer-Verlag, New York, 2008.

[47] DC Lagoudas, PB Entchev, P Popov, E Patoor, LC Brinson, and X Gao. Shape memory alloys, part ii: Modeling of polycrystals. *Mechanics of Materials*, 38(5):430–462, 2006.

[48] DC Lagoudas, DJ Hartl, Y Chemisky, L Machado, and P Popov. Constitutive model for the numerical analysis of phase transformation in polycrystalline shape memory alloys. *International Journal of Plasticity*, 32:155–183, 2012.

[49] S Lupi, M Forzan, and A Aliferov. *Induction and Direct Resistance Heating*. Springer, 2015.

[50] JH Mabe, B Fischer, and DJ Hartl. Characterization and modeling of trained nitinol torsional actuators under reverse bias loads. *TMS2013 Supplemental*

Proceedings, pages 987–998.

[51] JH Mabe, RT Ruggeri, E Rosenzweig, and MY Chin-Jye. Nitinol performance characterization and rotary actuator design. In *Smart Structures and Materials*, pages 95–109. International Society for Optics and Photonics, 2004.

[52] S Maeda, K Abe, K Yamamoto, O Tohyama, and H Ito. Active endoscope with SMA (shape memory alloy) coil springs. In *Micro Electro Mechanical Systems, 1996, MEMS'96, Proceedings. An Investigation of Micro Structures, Sensors, Actuators, Machines and Systems. IEEE, The Ninth Annual International Workshop on*, pages 290–295. IEEE, 1996.

[53] R Mirzaeifar, R DesRoches, and A Yavari. Exact solutions for pure torsion of shape memory alloy circular bars. *Mechanics of Materials*, 42(8):797–806, 2010.

[54] R Mirzaeifar, R DesRoches, A Yavari, and K Gall. Coupled thermo-mechanical analysis of shape memory alloy circular bars in pure torsion. *International Journal of Non-Linear Mechanics*, 47(3):118–128, 2012.

[55] R Mohr, K Kratz, T Weigel, M Lucka-Gabor, M Moneke, and A Lendlein. Initiation of shape-memory effect by inductive heating of magnetic nanoparticles in thermoplastic polymers. *Proceedings of the National Academy of Sciences of the United States of America*, 103(10):3540–3545, 2006.

[56] SA Morrison, CL Cahill, EE Carpenter, S Calvin, R Swaminathan, ME McHenry, and VG Harris. Magnetic and structural properties of nickel zinc ferrite nanoparticles synthesized at room temperature. *Journal of Applied Physics*, 95(11):6392–6395, 2004.

[57] Bobak Mosadegh, Panagiotis Polygerinos, Christoph Keplinger, Sophia Wennstedt, Robert F Shepherd, Unmukt Gupta, Jongmin Shim, Katia Bertoldi,

Conor J Walsh, and George M Whitesides. Pneumatic networks for noft robotics that actuate rapidly. *Advanced Functional Materials*, 24(15):2163–2170, 2014.

[58] SC Nian, MS Huang, and TH Tsai. Enhancement of induction heating efficiency on injection mold surface using a novel magnetic shielding method. *International Communications in Heat and Mass Transfer*, 50:52–60, 2014.

[59] V Novák, P Šittner, GN Dayananda, FM Braz-Fernandes, and KK Mahesh. Electric resistance variation of niti shape memory alloy wires in thermomechanical tests: Experiments and simulation. *Materials Science and Engineering: A*, 481:127–133, 2008.

[60] SD Oehler. *Developing Methods for Designing Shape Memory Alloy Actuated Morphing Aerostructures*. Texas A&M University, 2012.

[61] SD Oehler, DJ Hartl, and DC Lagoudas. Analysis and optimization of improved hybrid SMA flexures for high rate actuation. In *SPIE Smart Structures and Materials+ Nondestructive Evaluation and Health Monitoring*, pages 797907–797907. International Society for Optics and Photonics, 2011.

[62] K Otsuka and CM Wayman. *Shape Memory Materials*. Cambridge University Press, 1999.

[63] A Pathak, D Brei, and J Luntz. Experimental characterization of the convective heat transfer from shape memory alloy wire to various ambient environments. *Students papers, Pathak, A.; Mechanical Engineering, University of Michigan*, 2250:48109–2126, 2008.

[64] E Patoor, DC Lagoudas, PB Entchev, LC Brinson, and X Gao. Shape memory alloys, part i: General properties and modeling of single crystals. *Mechanics of Materials*, 38(5):391–429, 2006.

[65] H Prahlad and I Chopra. Design of a variable twist tilt-rotor blade using shape memory alloy (SMA) actuators. In *SPIE's 8th Annual International Symposium on Smart Structures and Materials*, pages 46–59. International Society for Optics and Photonics, 2001.

[66] MA Qidwai and DC Lagoudas. Numerical implementation of a shape memory alloy thermomechanical constitutive model using return mapping algorithms. *International Journal for Numerical Methods in Engineering*, 47(6):1123–1168, 2000.

[67] J Qiu, J Tani, D Osanai, Y Urushiyama, and D Lewinnek. High-speed response of SMA actuators. *International Journal of Applied Electromagnetics and Mechanics*, 12(1):87–100, 2000.

[68] J Roh, J Han, and I Lee. Finite element analysis of adaptive inflatable structures with SMA strip actuator. In *Smart structures and materials*, pages 460–471. International Society for Optics and Photonics, 2005.

[69] V Rudnev, D Loveless, RL Cook, and M Black. *Handbook of Induction Heating*. CRC Press, 2002.

[70] RS Ruffini, RT Ruffini, and VS Nemkov. Advanced design of induction heat treating coils - part ii: Magnetic flux concentration and control. *Industrial Heating*, 65(11):69–72, 1998.

[71] RS Ruffini, RT Ruffini, VS Nemkov, and RC Goldstein. Enhancing induction heating processes by applying magnetic flux controllers. In *19 th ASM Heat Treating Society Conference and Exposition including Steel Heat Treating in the New Millenium: An International Symposium in Honor of Professor George Krauss*, pages 162–167, 1999.

[72] RT Ruffini, V Nemkov, and N Vyshinskaya. New magnetodielectric materials for magnetic flux control. In *Proc. of Int. Symposium HES-04,Heating by Electromagnetic Sources, Padua, Italy*, 2004.

[73] M Sadiku. *Elements of Electromagnetics*. Oxford University Press, USA, 2014.

[74] B Sanders, R Crowe, and E Garcia. Defense advanced research projects agency–smart materials and structures demonstration program overview. *Journal of Intelligent Material Systems and Structures*, 15(4):227–233, 2004.

[75] JO Sanders, AE Sanders, R More, and RB Ashman. A preliminary investigation of shape memory alloys in the surgical correction of scoliosis. *Spine*, 18(12):1640–1646, 1993.

[76] RN Saunders, J Herrington, L Hodge, DJ Hartl, and JH Mabe. Optimization of a composite morphing wing with shape memory alloy torsional actuators. In *ASME Smart Materials, Adaptive Structures and Intelligent Systems*. American Society of Mechanical Engineers, 2014.

[77] SL Semiatin. *Elements of Induction Heating: Design, Control, and Applications*. ASM International, 1988.

[78] M Sreekumar, M Singaperumal, T Nagarajan, M Zoppi, and R Molfino. Recent advances in nonlinear control technologies for shape memory alloy actuators. *Journal of Zhejiang University SCIENCE A*, 8(5):818–829, 2007.

[79] TT Srinivasan, P Ravindranathan, LE Cross, R Roy, RE Newnham, SG Sankar, and KC Patil. Studies on high-density nickel zinc ferrite and its magnetic properties using novel hydrazine precursors. *Journal of Applied Physics*, 63(8):3789–3791, 1988.

[80] B Sun, J Zhang, X Wu, and W Liao. Single-joint driving system of bionic finger based on shape memory alloy. In *Micro-NanoMechatronics and Human Science (MHS), 2012 International Symposium on*, pages 225–228. IEEE, 2012.

[81] M Tabesh, BT Lester, DJ Hartl, and DC Lagoudas. Influence of the latent heat of transformation and thermomechanical coupling on the performance of shape memory alloy actuators. In *ASME 2012 Conference on Smart Materials, Adaptive Structures and Intelligent Systems*, pages 237–248. American Society of Mechanical Engineers, 2012.

[82] T Takagi, Y Luo, S Suzuki, M Matsumoto, and J Tani. Modeling and numerical simulation onthermomechanical behavior of SMA plates with two-way shape memory effect. *Journal of Intelligent Material Systems and Structures*, 12(11):721–728, 2001.

[83] M Tanaka, F Wang, K Abe, Y Arai, H Nakagawa, and S Chonan. A closed-loop transcutaneous power transmission system with thermal control for artificial urethral valve driven by SMA actuator. *Journal of intelligent material systems and structures*, 17(8-9):779–786, 2006.

[84] HF Tiersten. Energy and momentum in the electromagnetic field. In *A Development of the Equations of Electromagnetism in Material Continua*, pages 105–112. Springer, 1990.

[85] TL Turner, CL Lach, and RJ Cano. Fabrication and characterization of sma hybrid composites. In *SPIE's 8th Annual International Symposium on Smart Structures and Materials*, pages 343–354. International Society for Optics and Photonics, 2001.

[86] J Van Humbeeck. Non-medical applications of shape memory alloys. *Materials Science and Engineering: A*, 273:134–148, 1999.

[87] RT Watkins, JA Shaw, and DS Grummon. Shape memory thermal lag and superelastic rate sensitivity of SMA cellular structures. In *SPIE Smart Structures and Materials+ Nondestructive Evaluation and Health Monitoring*, pages 86890R–86890R. International Society for Optics and Photonics, 2013.

[88] J Webster. Shape memory material actuation, June 29 2005. US Patent App. 11/168,545.

[89] JB Westgard. *Electrodynamics a Concise Introduction*. Springer, 1996.

[90] ED Wetzel. Article and method for controlled debonding of elements using shape memory alloy actuators, August 10 2004. US Patent 6,773,535.

[91] T Zhu, P Feng, X Li, F Li, and Y Rong. The study of the effect of magnetic flux concentrator to the induction heating system using coupled electromagnetic-thermal simulation model. In *Mechanical and Automation Engineering (MAEE), 2013 International Conference on*, pages 123–127. IEEE, 2013.

APPENDIX A

CONVECTION COOLING STUDY

To calculate a convection coefficient, the flow in the tube must be determined to be laminar or turbulent and the degree to which is it developed (i.e. hydrodynamically developed, thermally developed, or fully developed) must be known. In order for flow to become fully developed, the fluid must travel up to 80 times the inlet diameter, which in the tube used is not possible. The vast majority of analytical solutions for tube and pipe flow rely on the assumption that the flow is developed so it is likely that any solution found for the convection coefficient may not be accurate.

Coolant flows through a radiator during cooling so that the sink temperature remains steady at 24 deg C. To determine whether the flow is laminar or turbulent, the Reynolds number is determined as

$$Re = \frac{V d_i}{\nu} \tag{A.1}$$

where V is the velocity of the flow, d_i is the inner diameter of the tube, and ν is the kinematic viscosity. The velocity is found as $Q/\frac{\pi}{4}d_i^2$ where Q is the volumetric flow rate. The kinematic viscosity was taken from [39] at the measured sink temperature. The Reynolds number of this flow was found to be turbulent so the convection coefficient was found from the Dittus-Boelter equation as

$$\frac{h d_i}{k} = 0.023 Re^{0.8} Pr^{0.3} \tag{A.2}$$

where the left hand side represents the Nusselt number and Pr is the Prandtl number.

The Prandtl number and thermal conductivity were again taken from [39] at the sink temperature. These calculations give a convection coefficient of 6800 W/(deg C m^2). In calculating this convection coefficient it was assumed that the flow temperature remains close to the sink temperature, that the convection coefficient does not change, and that the flow is fully developed. By application of a lumped-heat-capacity analysis [36], the feasibility of a constant temperature assumption can be determined. The temperature as a function of time, t, is given by

$$T(t) = T_w + (T_0 - T_w) \exp^{-t/\tau} \tag{A.3}$$

where $T(t)$ is the temperature at t, t, T_w and T_0 are the wall and sink temperature respectively, and τ is the time constant found as $\rho c d_i/(4h)$ where ρ is the density and c is the specific heat. Again the specific heat and density were taken from [39]. The time was found from the velocity and length of the tube, the sink temperature used was as measured from experiment, and the wall temperature used was measured from the FE model. This simplified equation predicts that the temperature of the coolant could increase by approximately 10 deg C by the time it reaches the end of the tube. Therefore use of the Dittus-Boelter equation with its stated assumptions produces the expectedly poor result shown in figure 4.6, which is not in good agreement with the experiment.

Rather than moving to a fluid dynamics simulation, a parametric study to determine a convection coefficient that could describe the cooling process was completed. The study assumed the flow enters the tube at the sink temperature and leaves the tube 10 deg C above the sink temperature. This change in temperature over the length of the tube is consistent with the result of the previous lumped-heat-capacity analysis. It is assumed that the temperature varies linearly along the length of the

tube from the sink temperature to the exit temperature. The parametric study varied the convection coefficient from 500 W/(deg C m^2) to 2500 W/(deg C m^2) in increments of 200. A sampling of this study is shown in figure A.1. The study

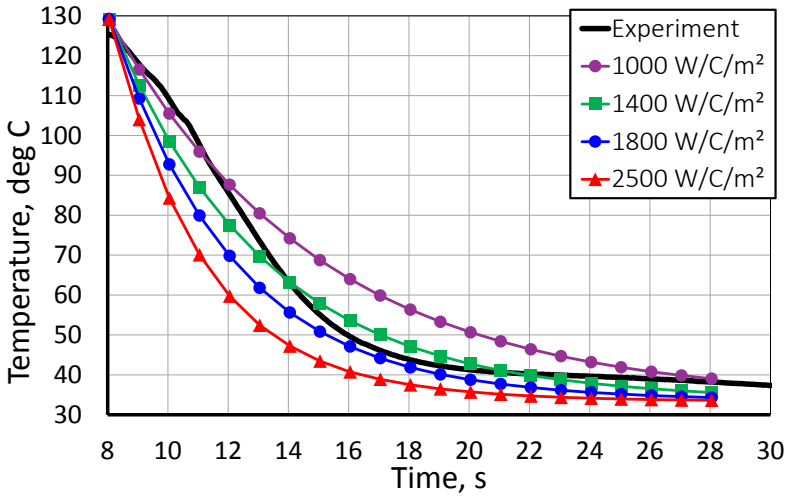

Figure A.1: Sample of the parametric study results to determine the effective convection coefficient in the high rate actuation study.

shows that the convection coefficient should be approximately 1400 W/(deg C m^2), which is significantly lower than the calculated value of 6800 W/(deg C m^2) shown in figure 4.6. The convection coefficient found from the parametric study is close to what has been observed from [39] for similar conditions. While the calculated value is high compared to the parametric study value it is still within a range of values that this fluid mixture could produce. A parametric study is not the ideal method to calculate the cooling coefficients, but it does provide useful data for studies that use this particular high rate actuation setup for future experiments.